CHAPTER 4

Mechanistic insights into Pd_mCu_n Clusters: Implication to the CO_2 Hydrogenation

4.1 Introduction

Palladium (Pd) nanoclusters with a precise number of atoms exhibit a range of fascinating structural, electronic, vibrational, and catalytic properties, which are unexpected from their bulk counterparts of Pd [1–5]. The diverse contradiction in properties of Pd nanoclusters from their bulk counterpart is attributed to the variety of factors such as high specific surface area, electronic shell closing (i.e., Jellium model) and geometric shell enclosing, super atomic character (the sharing of electrons between atoms is not same compared to their bulk systems) and quantum confinement. Due to their low cost and abundance with better thermal stability, Pd nanoclusters are unarguably the most active frontiers for their utilization in industrial chemistry and heterogeneous catalyst [6–10]. To date, many experimental and theoretical studies on Pd nanoclusters [11,12] have been carried out to develop an in-depth understanding of their minimum energy configurations for their utilization in hydrogen storage [13], oxidation, and reduction processes [14,15], and hydrogenation [16]. The adsorption energetics, dissociation, and electron transfer properties of CO, NO, H_2, etc., gas molecules over Pd nanoclusters have been successfully examined using density functional theory (DFT) based calculations [17–20]. Correspondingly, Sousa et al. [21] revealed that the Pd is a very sensitive catalyst in creating intermetallic bonds. Notably, it is observed that the tailoring of catalytic, electronic, magnetic, and optical properties can be achieved through the minor changes in the size, varying the chemical composition and order of constituent atoms of Pd bimetallic nanoclusters [22]. For instance, the recent advancement in the DFT calculations and experimental fabrications demonstrated that the impurity/doping can strongly influence the stability and physicochemical properties of the host clusters i.e., Pd-Ag [22], Pd-Co [23], Cu-Ni [24], Cu-V, etc. [25]. Mu et al. [26] found that the doping of the Mn atom enhances the structural stability and magnetic moment of the Pd clusters. The Pd bimetallic nanoclusters with a transition metal such as copper (Cu) with various structural configurations and compositions are being

explored by many researchers for their applications in oxygen reduction, oxidation of alcohol, oxidation reactions of formic acid, etc. [27–29]. It has been reported by Wu et al. [27] that the Cu atom in the Pd–Cu clusters enhance the catalytic activity. Saputro et al. [30] found that the adsorption strength of CO_2 with pure Pd clusters enhances after the doping of transition metals (M= Ni, Cu, Pt, Rh) and predicted that the Pd_6M clusters facilitate CO_2 hydrogenation for the production of HCOO/COOH. Though, there exist many studies on Pd-Cu bimetallic clusters [27–30]; very little is known about the atomic level morphology of Pd-Cu nanoalloy. To the best of our knowledge, icosahedral (I_h) Pd_mCu_n clusters (where m + n = 13) with different compositions of Cu atoms in the same structure and their sensitivity towards CO_2 adsorption are not yet addressed in the literature. Therefore, it is interesting to explore the impact of Cu doping on structural stability, electronic and vibrational properties (Raman spectra) along with their reactivity with CO_2 molecule over I_h Pd_mCu_n clusters. Hunting stable structures for bimetallic clusters is a difficult job due to the structural complexity present in them. Therefore, in the search of the possible low-lying geometries of clusters/alloys, a study must rely on the effective DFT approach. In this work, we concentrate on the I_h Pd_mCu_n clusters (where m + n = 13) with an interest to understand the role of Cu atom doping on the structural stability, electronic and vibrational properties. Hence, we first obtained the minimum energy configurations and then calculated the electronic and vibrational properties (Raman spectra) of I_h Pd_mCu_n clusters using DFT-based first-principles calculations. Followed by the investigation and analysis of the energetics of CO_2 molecule over I_h Pd_mCu_n clusters.

4.2 Computational details

All calculations for I_h Pd_mCu_n clusters (where m + n = 13) were performed by adopting Kohn Sham (KS) DFT method using Quantum ESPRESSO code [31]. The projected augmented-wave (PAW) type pseudopotentials were used to model the

electron-ion interaction [32]. The exchange-correlation energies were calculated within the generalized gradient approximation (GGA) using the Perdew-Burke-Ernzerhof (PBE) functional [33]. The kinetic energy cut-off for the description of the wave function in the plane-wave basis was set to 45 Ry. The electronic levels were broadened with Marzari-Vanderbilt smearing [34] of 0.01 Ry to improve the convergence for metallic clusters. To avoid the interaction between periodic images, I_h Pd_mCu_n clusters were placed in a large cubic supercell of 15 Å × 15 Å × 15 Å for the optimization. All Pd and Cu atoms residing in the I_h Pd_mCu_n clusters were allowed to relax. The first Brillouin zone (BZ) sampling was restricted to the gamma (Γ) point. The position of atoms in the I_h Pd_mCu_n clusters were fully optimized until the interatomic forces were smaller than 0.001 eV/Å using the Broyden-Fletcher-Goldfarb-Shanno (BFGS) algorithm [35]. Adsorption of CO_2 was assessed with four different geometries oriented towards the I_h Pd_mCu_n clusters. We used the same exchange-correlation functional and other computational parameters employed for optimizing the I_h Pd_mCu_n clusters. However, GGA functional failed to account for long-range van der Waals (vdW) interaction and lead to severe self-interaction (SI) errors [36]. Thus, to calibrate the accurate description of the long-range interactions between CO_2 molecule and I_h Pd_mCu_n clusters, we introduced the vdW correction proposed by Grimme, namely the D2 framework [37]. All calculations were performed in non-spin polarized condition because all the adsorbed structures (CO_2/Pd_mCu_n) clusters were found to be in a nonmagnetic state. To confirm the nonmagnetic state, we performed the spin-polarized calculations which indicate the non-significant impact of spin polarization on adsorption energies. Noteworthy, analysis of vibrational properties of I_h Pd_mCu_n clusters have been carried out using the DFT method as encoded in the GAUSSIAN09 package [38]. For the calculation of vibrational frequencies using the GAUSSIAN09 code, we used the same optimized geometrical parameters which were obtained from Quantum ESPRESSO code. The hybrid exchange-correlation functional B3LYP/LanL2MB (an effective core potential basis set) is used

[39, 40]. The spin state is singlet for I_h Pd_{13} and Pd_mCu_n clusters (even electron clusters with an even number of Cu atoms). However, it is doublet for I_h Cu_{13} and Pd_mCu_n clusters (odd electron clusters with an odd number of Cu atoms) without imposing any symmetry constraints.

4.3 Results and Discussion

4.3.1 Structural stability and electronic properties of I_h Pd_mCu_n clusters

In this section, we present and discuss the most stable structure and electronic properties of I_h Pd_mCu_n clusters (where m + n = 13). We primarily optimized the pristine Cu_{13} and Pd_{13} clusters. It is found that the Pd_{13} and Cu_{13} clusters prefer the icosahedral configuration after optimization which is consistent with previous works [19, 41]. The systematically determined optimized geometries of I_h Pd_mCu_n clusters (where m + n = 13) are presented in Figure 4.1. From Figure 4.1, one can see that the ground state geometry of I_h Pd_mCu_n clusters are analogous to I_h Cu_{13} and Pd_{13} clusters. Our results are consistent with the previous literature on doped bimetallic clusters [24]. It can also be seen from Figure 4.1 that the Cu atom prefers to stay at the "core" of the clusters while the Pd atom desires more to get distributed over the surface of clusters [24]. The structural stability of I_h Pd_mCu_n clusters is examined by calculating the average binding energy per atom and mixing energy. The average binding energy per atom for pure and bimetallic clusters has been calculated using the following expressions,

$$E_b(Pd_m) = \frac{[m \times E(Pd) - E(Pd_m)]}{m} \tag{4.1}$$

$$E_b(Pd_mCu_n) = \frac{[(m) \times E(Pd) + E(Cu) - E(Pd_mCu_n)]}{(m+n)} \tag{4.2}$$

$$E_b(Cu_n) = \frac{[n \times E(Cu) - E(Cu_n)]}{n} \tag{4.3}$$

where $E(Pd_m)$, $E(Pd_mCu_n)$ and $E(Cu_n)$ represent the total energy of the lowest-energy structures of I_h Pd_{13}, Pd_mCu_n and Cu_{13} clusters, respectively. The $E(Pd)$ and $E(Cu)$ represents the atomic energy of isolated Pd and Cu atoms, respectively.

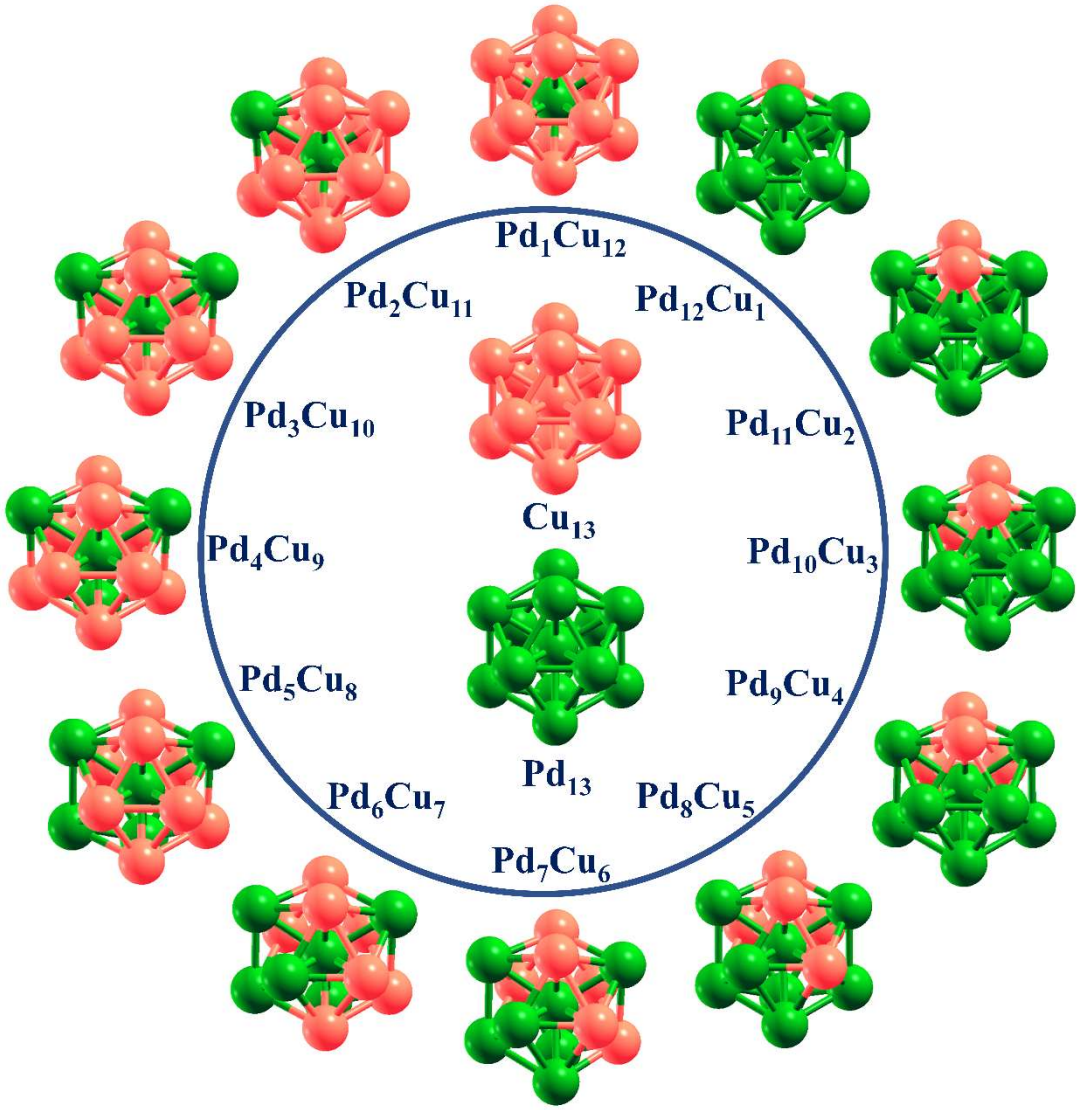

Figure 4.1: The optimized configuration of I_h Pd_mCu_n (m + n = 13) clusters with different Cu compositions.

The calculated average binding energy per atom of stable I_h Pd_mCu_n clusters is plotted in Figure 4.2 and quantified in Table 4.1. The calculated average binding energy per atom for I_h Pd_{13} and Cu_{13} clusters is 2.47 eV and 2.78 eV respectively which agrees well with the previously reported data [19,42]. Figure 4.2 depicts that the I_h Cu_{13} cluster is more stable than I_h Pd_{13} cluster. Analysis of these results indicate that the most stable I_h bimetallic cluster is Pd_5Cu_8 with 2.88 eV average binding energy per atom while I_h $Pd_{12}Cu$ cluster is the least stable bimetallic cluster with a 2.53 eV average binding energy per atom. Our results also suggest that the I_h clusters containing Cu

atoms are more stable than the I_h Pd_{13} cluster which indicates that the doping of Cu atoms improve the binding energy of clusters.

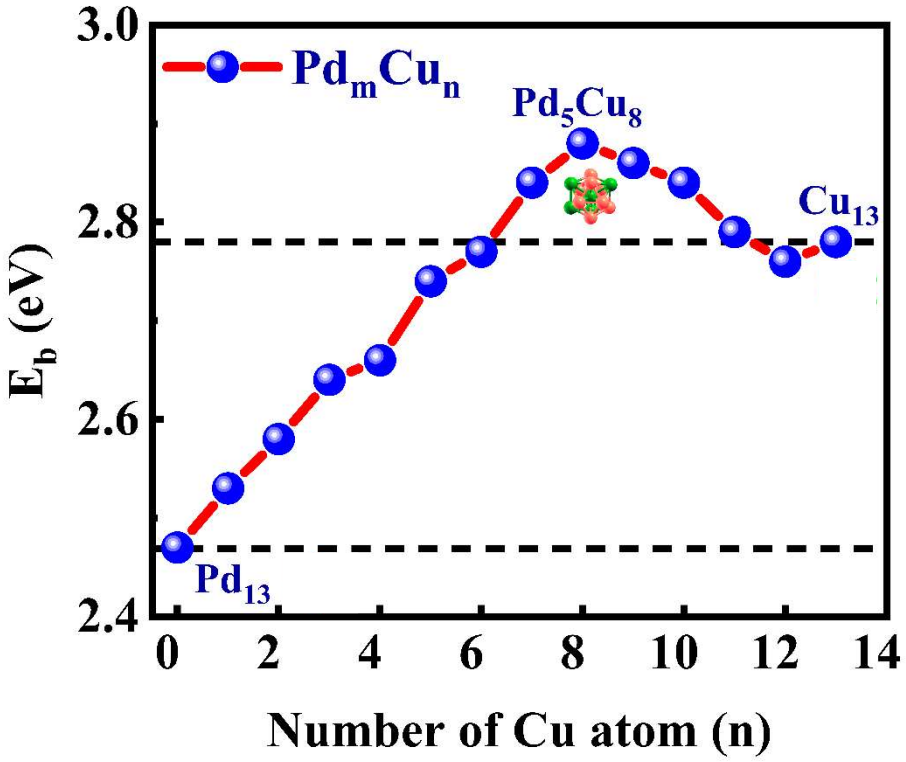

Figure 4.2: Average binding energy per atom (E_b eV) of I_h Pd_mCu_n (m + n = 13) clusters with a different numbers of Cu atoms.

To estimate the relative stability of the I_h Pd_mCu_n clusters, the mixing energy E_{mix} [43–45] adapted by bimetallic clusters is expressed by the following expression,

$$E_{mix} = \frac{1}{13}\left[E(Pd_mCu_n) - \frac{m}{13}E(Pd_{13}) - \frac{n}{13}E(Cu_{13})\right] \quad (4.4)$$

where $E(Pd_mCu_n)$, $E(Pd_{13})$ and $E(Cu_{13})$ are the total energy of I_h Pd_mCu_n, pristine Pd_{13} and pristine Cu_{13} clusters, respectively. The mixing energy is the measure of the energy gain for the bimetallic clusters with respect to the segregated phase consisting of two independent clusters of $\frac{m}{13}E(Pd_{13})$ *and* $\frac{n}{13}E(Cu_{13})$. It is clear from Eqn. (4.4) that the mixing energy of pure extremes is always zero. However, its negative value points out the thermodynamical stability of the formation/composition of alloys. The calculated mixing energy of I_h Pd_mCu_n clusters is shown in Table 4.1.

Table 4.1: The average binding energy per atom (E_b eV), mixing energy (E_{mix} eV), second-order energy difference (Δ^2E eV), and average bond length ($\bar{R}$(Å)) of I_h Pd_mCu_n (m + n = 13) clusters.

Cluster	E_b	E_{mix}	Δ^2E	$\bar{R}$
Pd_{13}	2.47	0.0	N.A.	2.76
$Pd_{12}Cu$	2.53	-0.03	0.05	2.74
$Pd_{11}Cu_2$	2.58	-0.06	-0.005	2.73
$Pd_{10}Cu_3$	2.64	-0.09	0.45	2.70
Pd_9Cu_4	2.66	-0.09	-0.85	2.66
Pd_8Cu_5	2.74	-0.15	0.67	2.66
Pd_7Cu_6	2.77	-0.16	-0.45	2.65
Pd_6Cu_7	2.84	-0.20	0.36	2.64
Pd_5Cu_8	2.88	-0.22	0.68	2.64
Pd_4Cu_9	2.86	-0.18	0.16	2.62
Pd_3Cu_{10}	2.84	-0.13	0.26	2.60
Pd_2Cu_{11}	2.79	-0.06	-0.19	2.60
$PdCu_{12}$	2.76	-0.01	-0.58	2.60
Cu_{13}	2.78	0.0	N.A.	2.52

The maximum negative value of the mixing energy corresponds to the most stable alloyed cluster for the given size. On the other hand, a positive value of the mixing energy will characterize a tendency of segregation among the two species of constituent atoms. It is found that the mixing energy is negative for all I_h Pd_mCu_n clusters and revealing that the alloy formation favors to form the whole range of compositions of the I_h Pd_mCu_n clusters. The higher magnitude of negative E_{mix} value indicates more favorable mixing. Therefore, it is concluded that the introduction of Cu atoms into Pd clusters makes the formation of binary clusters more favorable. It is in agreement with

the reported results of mixing energy investigated for Ni-doped I_h Cu_{13} clusters [24]. Our results point out that the mixing energy reaches the minimum value (−0.22 eV) for the I_h Pd_5Cu_8 cluster indicating that this composition corresponds to the magic composition with the highest stability. This corroborates with the results of the average binding energy per atom. It is noteworthy that the I_h $PdCu_{12}$ cluster has a minimum negative value (−0.01 eV) in the group of bimetallic clusters indicating that the mixing of I_h $PdCu_{12}$ bimetallic cluster is least favorable.

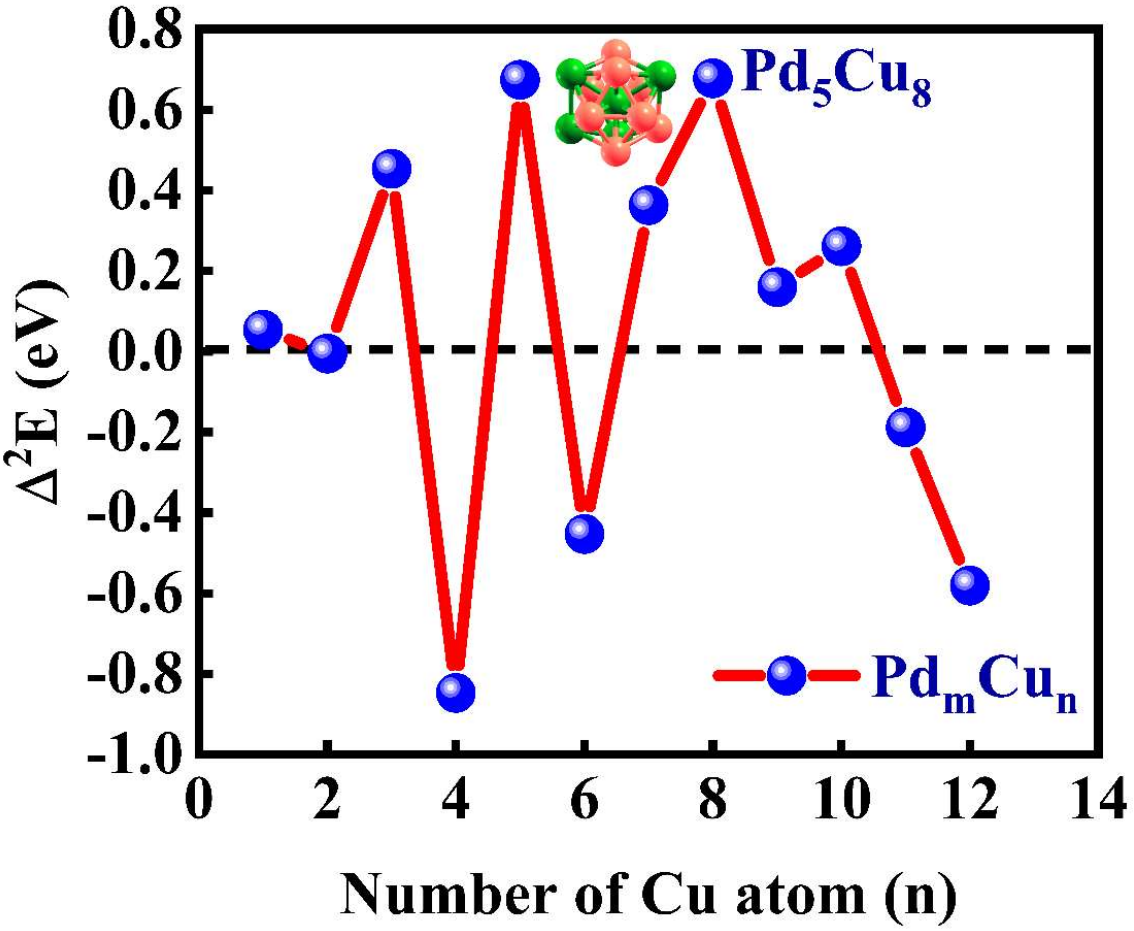

Figure 4.3: Second order energy difference (Δ^2E eV) of I_h Pd_mCu_n (m + n = 13) clusters with a different numbers of Cu atoms.

Now we turn our attention to the second-order energy difference, which is a sensitive factor frequently used as a measure of the relative stability of a particular cluster with respect to adjacent sizes or compositions. It is often associated directly with

the relative abundances examined by mass spectroscopy experiments. The second-order energy difference of I_h Pd_mCu_n clusters is calculated as [43, 44] follows,

$$\Delta^2 E_{(Pd_mCu_n)} = E(Pd_{m+1}Cu_{n-1}) + E(Pd_{m-1}Cu_{n+1}) - (Pd_mCu_n) \quad (4.5)$$

where $E(Pd_{m+1}Cu_{n-1})$, $E(Pd_{m-1}Cu_{n+1})$ and $E(Pd_mCu_n)$ represent the total energy of the optimized $Pd_{m+1}Cu_{n-1}$, $Pd_{m-1}Cu_{n+1}$ and Pd_mCu_n clusters, respectively.

The calculated $\Delta^2 E$ as a function of Cu atoms in I_h Pd_mCu_n clusters for different compositions is shown in Figure 4.3. It is recognized that the maximum value of $\Delta^2 E$ relative to its immediate adjacent cluster indicates improved stability of a particular cluster. Therefore, the value of $\Delta^2 E$ can be considered as a complementary measure of the stability of clusters, where the most stable clusters are recognized from the maxima of $\Delta^2 E$. Conspicuous odd-even oscillations for I_h Pd_mCu_n clusters were not observed in Figure 4.3. Our result indicates that the presence of the Cu atom changes the stability of the host clusters. In I_h Pd_mCu_n clusters, the substitution of an odd number of Cu atoms shows greater stability as compared to the clusters which are composed with an even number of Cu atoms (except for 8 and 10). Moreover, several pronounced peaks are found at n=1, 3, 5, 7, 8, and 10, implying strong relative stability of clusters as compared to others. It is evident that the peaks corresponding to the $Pd_{10}Cu_3$, Pd_8Cu_5 and Pd_5Cu_8 clusters are relatively stable compared to their adjacent clusters. There is also a small peak indicate the stability is observed at n = 1 and 10. The Pd_5Cu_8 is the most stable binary cluster with the highest (0.678 eV) $\Delta^2 E$ and a noticeable intense peak (Figure 4.3). The results corresponding to the second-order energy difference of Pd_5Cu_8 cluster is also reflected in the calculated mixing energy and average binding energy per atom. Consequently, our results indicate that the Pd_5Cu_8 is the magic cluster and consumes a higher abundance in mass spectra.

The average bond length reflects the stability of the structure as it directly depends on bond energy. Henceforth, we have calculated the average bond length $\bar{R}$ of I_h Pd_mCu_n clusters using the following formula and presented in Figure 4.4.

$$\bar{R} = \frac{1}{N_{abl}} \sum_{i} R_{ij} \tag{4.6}$$

where R_{ij} is the distance between two bonded atoms and N_{abl} is the total number of bonds. The average Pd-Pd bond length of 2.75 Å in Pd_{13} cluster is the same as it is in bulk form. The obtained average bond length of I_h Pd_{13} cluster agrees well with the previously reported DFT work [19]. In contrast to this, the Cu–Cu average bond length of I_h Cu_{13} cluster (2.52 Å) is shorter by 0.04 Å as compared to its bulk form (2.56 Å). This significant decrease of the Cu–Cu average bond length of I_h Cu_{13} cluster results in higher average binding energy per atom. It is evident from Figure 4.4 that the bond length of the compositional clusters tends to shorten due to the greater specific surface area.

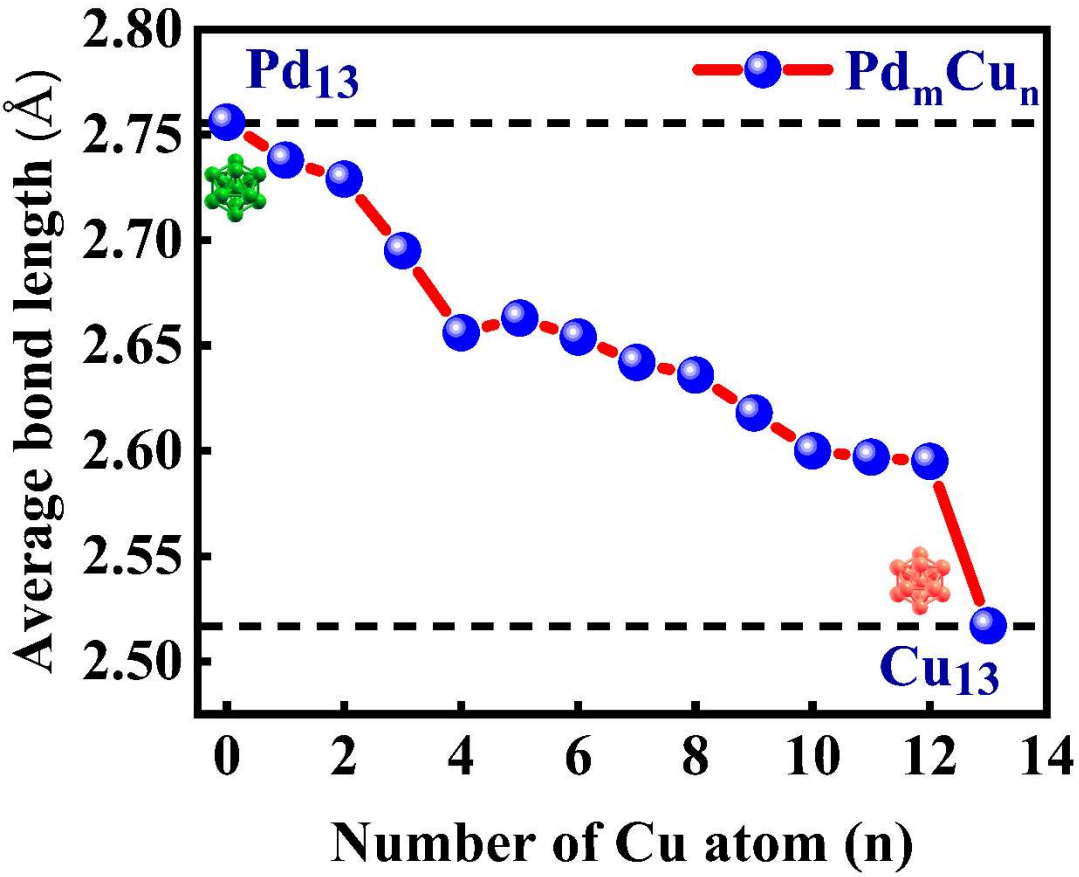

Figure 4.4: Average bond length $\bar{R}$ (Å) of I_h Pd_mCu_n (m + n = 13) clusters with different numbers of Cu atoms.

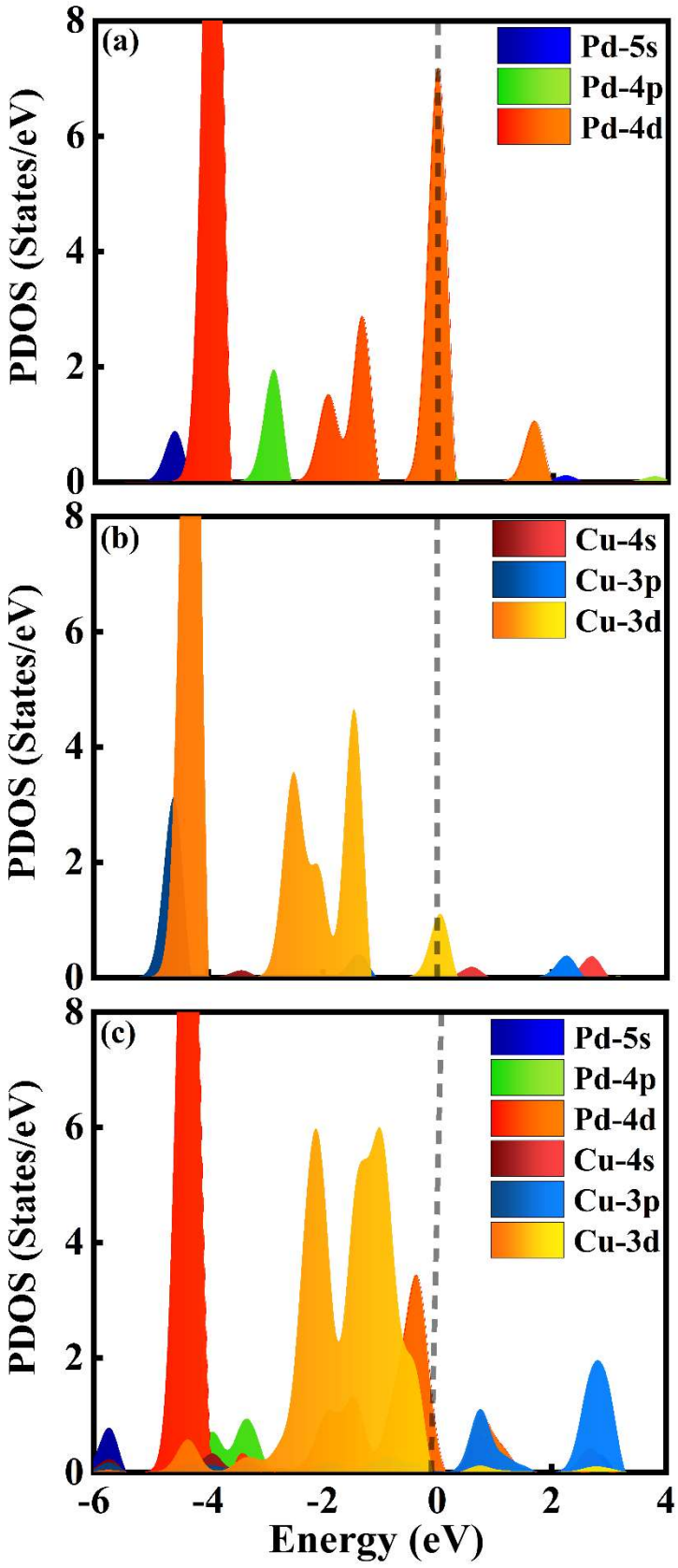

Figure 4.5: The PDOS of (a) Pd_{13}, (b) Cu_{13}, and (c) Pd_5Cu_8 clusters. The Fermi level is set to zero (black line).

The rapid change in the average bond length in the case of n = 1 (I_h $Pd_{12}Cu$ cluster) generally implies a variation in bonding and is more stable compared to I_h Pd_{13} cluster. The values of the average bond length of considered clusters are also presented in Table 4.1. To comprehend the modification in the electronic structure of the I_h Pd_{13} cluster due to Cu atom doping, we have carried out an analysis of the projected density of states (PDOS) and is presented them in Figure 4.5(a–c). For I_h Pd_{13} cluster, it is seen from Figure 4.5(a) that the Pd-4d orbitals are localized near the Fermi level (E_F). The contribution of Pd-5s orbitals is negligible (mainly below the Fermi level with a very small peak) as compared to Pd-4p and Pd-4d orbitals and it is consistent with the PDOS of I_h Pd_{13} cluster reported by Liu et al. [19]. In the case of I_h Cu_{13} cluster (Figure 4.5(b)), Cu-3p and Cu-3d orbitals largely contribute to the valence band region (below the Fermi level). Figure 4.5(b) reveals that the electronic states of Cu-3d orbitals below the Fermi level influence the stability of I_h Cu_{13} cluster with little contribution from the Cu-3p orbitals. This is consistent with the calculated results of structural stability of I_h Cu_{13} cluster. Similar to the I_h Pd_{13} cluster, the involvement of Cu-4s orbitals is quite less as compared to Cu-3p and Cu-3d orbitals. This gives a clear indication of strong hybridization between respective p and d orbitals in Pd and Cu clusters and a very small donation from s-states.

We thoroughly explored the PDOS of the Cu-doped Pd cluster (I_h Pd_5Cu_8 cluster) to understand the interaction mechanism of different orbitals (Figure 4.5(c)). It is seen that the substitution of the Cu atom results in the noteworthy increment of the electronic states in the locality of the Fermi level. Exclusively, the electronic states at the Fermi level of the Cu atom significantly increase. This alteration in the PDOS after introducing the Cu atom to the Pd-cluster is consistent with the PDOS of Cu-doped platinum clusters [46]. The Pd-4d peak shifts below the Fermi level, suggest strong hybridization between d-d orbitals. The modified orbital interaction gets going from pure to bimetallic clusters. The PDOS of I_h Pd_5Cu_8 cluster presented in (Figure 4.5(c)) shows

that the interaction mainly takes place between the d and p-orbitals, while, s orbitals of Pd and Cu atoms do not play any significant role. In I_h Pd_5Cu_8 cluster, 4p and 4d orbitals of Pd participates in the bonding process with the 3p and 3d orbitals of Cu. The stability of the Cu doped cluster is mainly dominated by Cu-3d orbitals with some contributions from 4s and 3p orbitals. The obtained results of PDOS reconfirm the calculated stability factors. On another front, the Löwdin charge assessment reveals the charges transfer from the Cu atom to the Pd atom in I_h Pd_mCu_n clusters which is primarily attributed to Pauling's electronegativity of the Pd atom (2.2) being higher as compared to the Cu atom (1.90). This charge transfer results in the alteration on electronic structures of the Pd as well as the surface chemical properties.

4.3.2 Raman spectra of I_h Pd_mCu_n clusters

To further examine the influence of step-by-step Cu doping on the vibrational properties of the Pd cluster, Raman spectra of I_h Pd_mCu_n clusters with B3LYP/LANL2MB level of DFT theory are calculated and displayed in Figure 4.6. For comparative analysis, the frequency corresponding to the high intense Raman active peak of I_h Pd_{13} cluster at 212 cm^{-1} is considered as a characteristic peak (see Figure 4.6(a)). It is clear from Figure 4.6(b–n) that the Cu doping in I_h Pd_mCu_n clusters result in a blue/red-shift of the characteristic peak. This blue/red-shift of the Raman characteristic peak after increase in the Cu doping can be attributed to the Pd-Cu bond length change arising from electron charge redistribution and change in chemical composition. The characteristic peak blue shifts to 312 cm^{-1}, 221 cm^{-1}, 225 cm^{-1}, 234 cm^{-1}, 240 cm^{-1}, 341 cm^{-1}, 246 cm^{-1}, 249 cm^{-1}, 251 cm^{-1}, 250 cm^{-1} and 486 cm^{-1} observed in the case of $Pd_{12}Cu$, $Pd_{11}Cu_2$, $Pd_{10}Cu_3$, Pd_9Cu_4, Pd_7Cu_6, Pd_6Cu_7, Pd_5Cu_8, Pd_3Cu_{10}, Pd_2Cu_{11}, $PdCu_{12}$ and Cu_{13} clusters respectively. However, a red-shift in the characteristic peak from 212 cm^{-1} to 179 cm^{-1} and 192 cm^{-1} is observed in the case of Pd_8Cu_5 and Pd_4Cu_9 clusters, respectively.

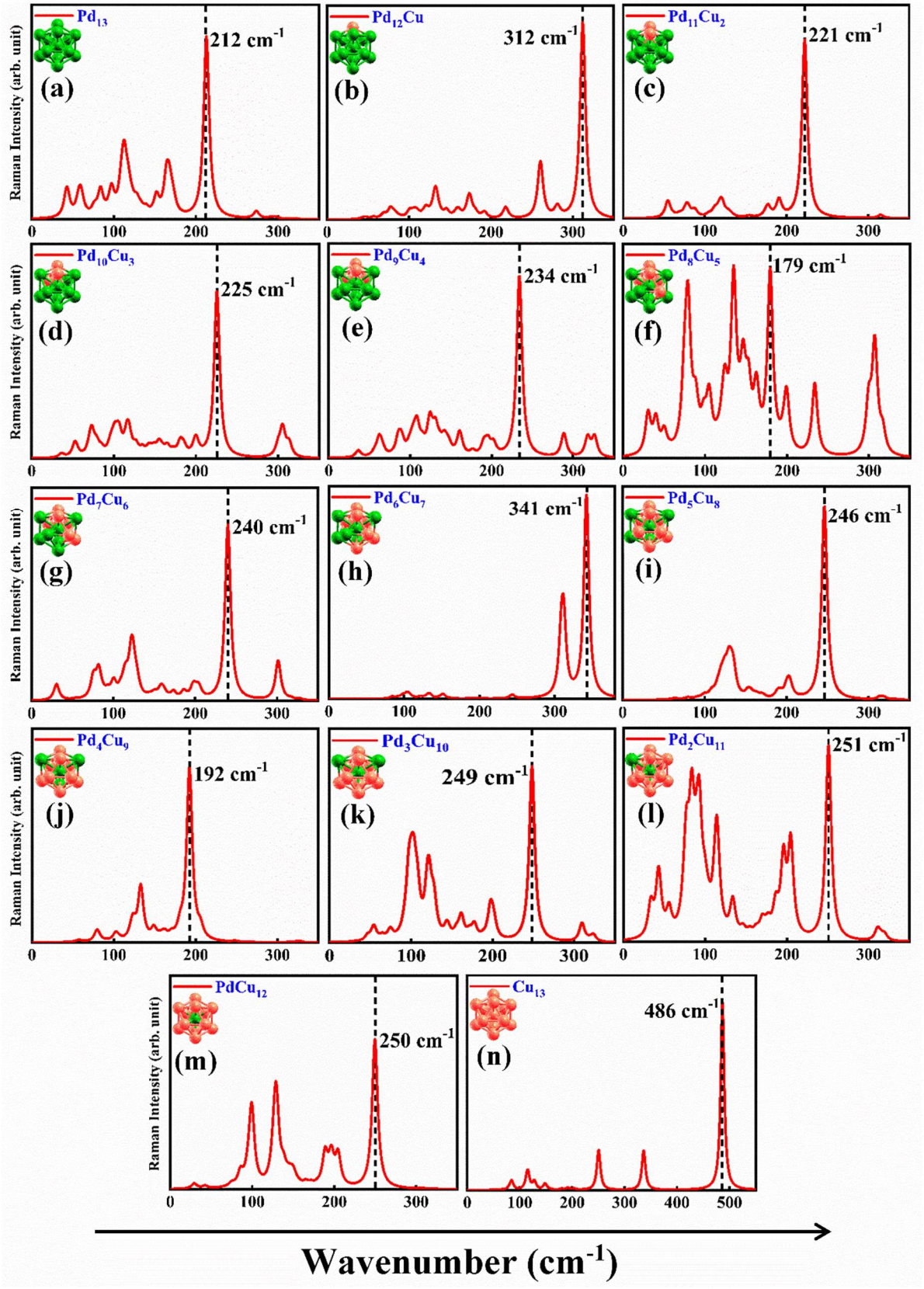

Figure 4.6: (a-n) Raman spectra of I_h Pd_mCu_n (m + n = 13) clusters.

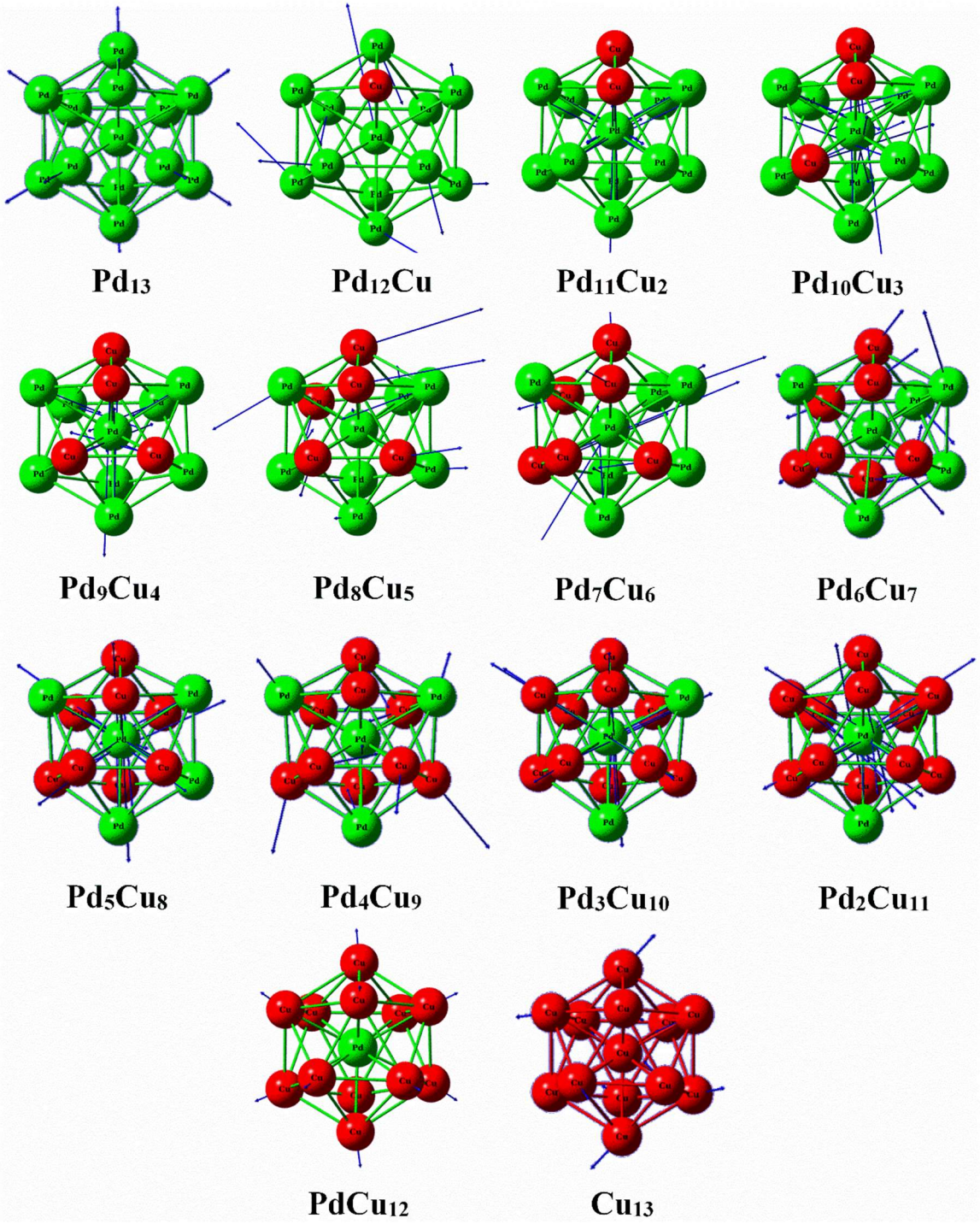

Figure 4.7: The vibrational mode of I_h Pd_mCu_n (m + n = 13) clusters corresponding to the high intense peak of their respective Raman spectra.

The vibrational mode corresponding to the most intense Raman active peak of I_h Pd_mCu_n clusters are presented in Figure 4.7. In the case of Pd_3Cu_{10}, Pd_2Cu_{11} and $PdCu_{12}$ clusters, the magnitude of blue-shift is nearly equal which can be attributed to the almost same average bond length. The maximum blue-shift in the characteristic

Raman peak is observed for the I_h Cu_{13} cluster which can be attributed to the significant decrease in the Cu–Cu bond length ad compared to its bulk counterpart. The smallest blue-shift in characteristic peak is observed in the case of $Pd_{11}Cu_2$ cluster.

4.3.3 Adsorption of CO_2 molecule over I_h Pd_mCu_n clusters

The bimetallic clusters have generated much interest for their excellent catalytic performance and reducing sensitivity for CO_2 poisoning [46]. One of the main goals of the present study is to understand the reactivity of CO_2 gas molecule over the Cu-doped Pd clusters. Therefore, we explored the effect of the different compositions (systematic doping of Cu atom) on the reactivity of a CO_2 molecule over I_h Pd_mCu_n clusters as compared to pristine I_h Pd_{13} and Cu_{13} clusters. Before adsorbing the CO_2 molecule over the I_h Pd_mCu_n clusters, initially we optimized the isolated CO_2 molecule keeping similar convergence criteria. The computed bond length ($R_{(C\text{-}O1/O2)}$ = 1.17 Å for CO_2) and bond angle ($\angle$O1-C-O2 = 180.0° for CO_2) are in excellent agreement with a previous report [47] which authenticates our computational method and gives assurance for further investigations. After that, we thoroughly accomplished the lowest-energy structural search for CO_2 adsorption over the low-lying structures of I_h Pd_mCu_n clusters. In this process, four kinds of adsorption models were considered for CO_2 adsorption over I_h Pd_mCu_n clusters namely, -OCo-, -oCO-, -OcO- and -OCO- as shown in Figure 4.8. The optimized structures of CO_2 adsorbed I_h Pd_mCu_n clusters with desired adsorption geometry are shown in Figure 4.9. We use Eqn. (4.7) to calculate the CO_2 adsorption energy over I_h Pd_mCu_n clusters,

$$E_{ads} = E_{(Pd_mCu_nCO_2)} - (E_{(Pd_mCu_n)} - E_{(CO_2)}) \quad (4.7)$$

where $E_{(Pd_mCu_nCO_2)}$, $E_{(Pd_mCu_n)}$ and $E_{(CO_2)}$ is the total energy of cluster after CO_2 adsorption, the energy of the free cluster ($E_{(Pd_mCu_n)}$ clusters), and the energy of an isolated CO_2 molecule in a vacuum, respectively. The computed adsorption energy and structural parameters of CO_2 molecule over I_h Pd_mCu_n clusters are listed in Table 4.2. Our results on the first three adsorption models of CO_2 adsorption over I_h Pd_mCu_n

clusters are similar to the case of CO_2 adsorption over I_h bimetallic Cu–Ni and Ni_{55} clusters [47]. Our study points out that -OcO- orientation is the most preferred adsorption configuration among Cu doped clusters. On another front, the CO_2 prefers -OCo- adsorption configuration to get adsorbed over I_h Pd_{13} and Cu_{13} clusters. Our results are consistent with the literature [47].

Table 4.2: Adsorption geometry, adsorption energy (E_{ads}, eV), structural parameters (distance between C–O1 (Å), C–O2 (Å), and ∠O1–C–O2 in degree) of adsorbed CO_2 molecule over I_h Pd_mCu_n (m + n = 13) clusters with Löwdin charge transfer (e) from cluster to an adsorbed CO_2 molecule.

Adsorption Geometry of CO_2	Cluster Composition	E_{ads} (eV)	Structural Parameters of CO_2			Löwdin Charge Transfer (e)
			C–O1	C–O2	∠O1–C–O2	
-OCo-	Pd_{13}	-7.00	1.25	1.23	138.7	0.19
-oCO-	$Pd_{12}Cu$	-7.00	1.23	1.25	139.1	0.18
-oCO-	$Pd_{11}Cu_2$	-6.62	1.22	1.25	139.5	0.19
-OCo-	$Pd_{10}Cu_3$	-6.70	1.26	1.23	137.8	0.18
-OcO-	Pd_9Cu_4	-6.36	1.23	1.22	143.7	0.09
-OcO-	Pd_8Cu_5	-5.86	1.23	1.23	144.1	0.09
-OcO-	Pd_7Cu_6	-5.95	1.23	1.22	144.3	0.09
-OcO-	Pd_6Cu_7	-5.63	1.23	1.23	144.0	0.09
-OcO-	Pd_5Cu_8	-5.56	1.23	1.23	144.3	0.09
-OcO-	Pd_4Cu_9	-6.12	1.23	1.23	144.4	0.09
-OcO-	Pd_3Cu_{10}	-6.65	1.24	1.24	139.7	0.22
-oCO-	Pd_2Cu_{11}	-6.86	1.22	1.28	133.3	0.28
-OCO-	$PdCu_{12}$	-6.98	1.27	1.27	126.9	0.40
-OCo-	Cu_{13}	-6.76	1.28	1.21	134.0	0.25

The charge transfer from substrate to the CO_2 molecule arising from the strong covalent interaction ultimately results in the linear to the bent transition of the CO_2 molecule with the elongation of the C–O bonds. More specifically, from Table 4.2, one can see that the I_h Pd_{13}, $Pd_{12}Cu$, $Pd_{11}Cu_2$, $Pd_{10}Cu_3$, Pd_3Cu_{10}, Pd_2Cu_{11}, $PdCu_{12}$, and Cu_{13} clusters exhibit strong CO_2 adsorption with higher adsorption energy in the range of -6.65 eV to -7.00 eV. The weak CO_2 interaction is observed in the case of Cu-doped clusters ranging from I_h Pd_9Cu_4 to Pd_4Cu_9 clusters. The Löwdin charge analysis has been performed to examine the charge transfer from clusters to CO_2 molecule and is depicted in Table 4.2. The clusters that possess adsorption energy (strong interaction) in between -6.65 eV to -7.00 eV have transferred 0.18 to 0.4 e charge to CO_2 molecule, while Pd_9Cu_4 to Pd_4Cu_9 clusters have transferred very little charge (0.09 e) to the CO_2 molecule. In comparison to the gas phase of the CO_2 molecule, C–O bonds elongate (1.23–1.26 Å), and the ∠O1-C-O2 angle decreases (<140°) in the case of strongly adsorbed CO_2 molecule over I_h Pd_mCu_n clusters. In the weakly adsorbed CO_2 molecule over Pd_9Cu_4 to Pd_4Cu_9 clusters, the bond angle (∠O1-C-O2) of the CO_2 molecule is around 144° and elongation in the bond distances is almost the same (1.22–1.23 Å). The computed bond angle and bond lengths of CO_2 molecule after adsorption are corroborating with our finding of CO_2 adsorption energy. The adsorption energy of CO_2 molecule (-OCo-) over I_h Pd_{13} and Cu_{13} clusters is 7.00 eV and -6.76 eV, respectively. This difference in the adsorption energy is also reflected in the C–O1 and C–O2 bond lengths. A similar situation is observed in the case of CO_2 adsorption over I_h Cu_{55} and Ni_{55} clusters [47]. The doping of a single Cu-atom in the Pd cluster ($Pd_{12}Cu$) does not affect the adsorption energy of CO_2 but its adsorption geometry (-oCO-) is different compared to the I_h Pd_{13} cluster. Further increasing the amount of Cu-doping, the CO_2 adsorption energy is found lesser as compared to I_h Pd_{13} cluster. The data depicted in Table 4.2 demonstrate that the Pd_9Cu_4 to Pd_3Cu_{10} clusters exhibit the same CO_2 adsorption geometry (-OcO-).

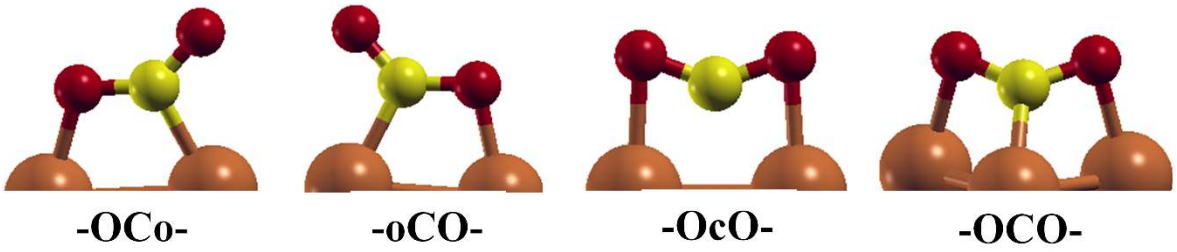

Figure 4.8: Different adsorption geometries for CO_2 adsorption over I_h Pd_mCu_n (m + n = 13) clusters.

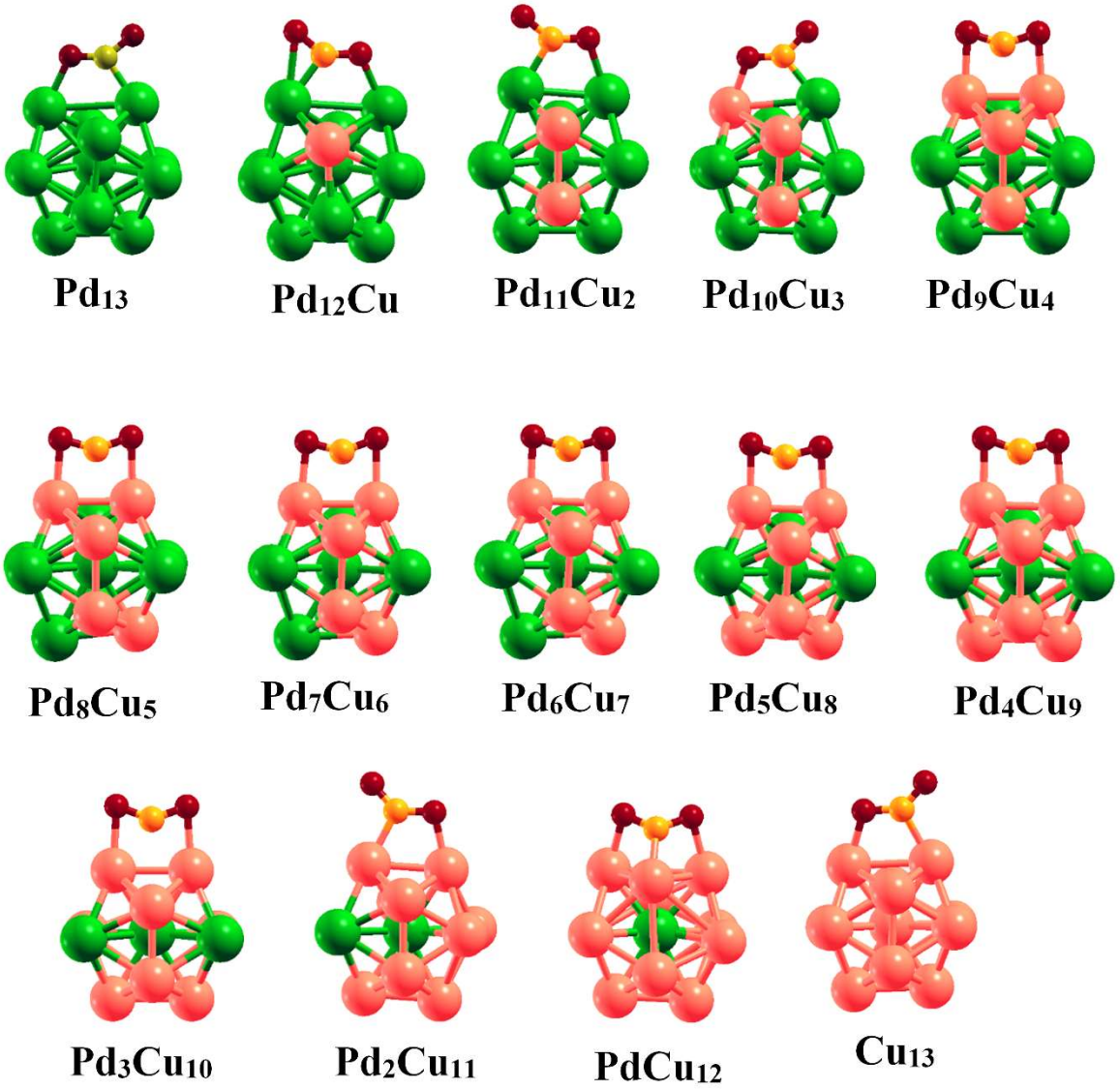

Figure 4.9: The CO_2 adsorbed I_h Pd_mCu_n (m + n = 13) clusters. The green, light pink, yellow, and red color sphere indicates Pd, Cu, C, and O atoms, respectively.

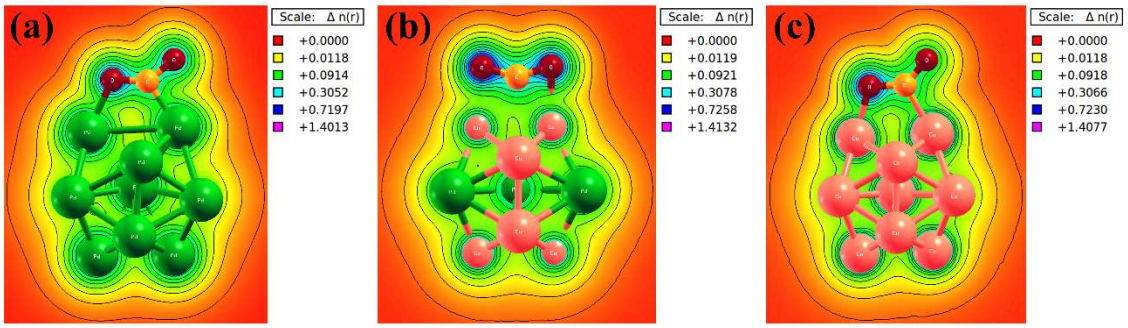

Figure 4.10: (a-c) Charge density plots of CO_2 adsorbed Pd_{13}, Pd_5Cu_8 and Cu_{13} clusters. The green, light pink, yellow, and red color sphere indicates Pd, Cu, C and O atoms, respectively.

It should be noted that only the $PdCu_{12}$ cluster exhibits the -OCO- geometry for the CO_2 adsorption (E_{ads} = 6.98 eV) with maximum charge transfer (0.4 e) from the cluster to the CO_2 molecule. The longest elongation in C–O1 and C–O2 (1.27 Å) bond length of adsorbed CO_2 molecule over $PdCu_{12}$ cluster confirms our results on adsorption energy and charge transfer. Figure 4.10 (a-c) shows the charge density plots of CO_2 molecule adsorbed over I_h Pd_{13}, Pd_5Cu_8 and Cu_{13} clusters, respectively. The electronegativity of Pd/Cu-atom for I_h Pd_{13}, Pd_5Cu_8 and Cu_{13} clusters is changing from 0.0914 to 0.0921. The maximum charge accumulated near the oxygen (O) atom (attached with cluster) is ~0.30 e in the case of Pd_{13} and Cu_{13} clusters. For the Pd_5Cu_8 cluster, ~0.72 e charge is accumulated around the O atoms. The accumulation of charge near the O atom suggests that the O atom plays a major role in CO_2 molecule adsorption as compared to carbon (C). The charge density plots also validate our findings on charge transfer from clusters to the CO_2 molecule. The adsorption energies indicate that the introduction of Cu atoms to Pd clusters decreases the adsorption ability of the clusters towards the CO_2 molecule.

4.3.4 CO_2 conversion into hydrocarbon fuels on I_h Pd_5Cu_8 cluster

Carbon dioxide (CO_2) hydrogenation to value-added fuels and chemicals such as formic acid (HCOOH), methanol (CH_3OH), and methane (CH_4) via heterogeneous catalysis, not only efficiently alleviates environmental issues caused by enormous CO_2

emissions but also reduces our excessive dependence on fossil fuels and generating good economic profits [48]. As carbon (C) is in its highest oxidation state in CO_2, its reduction and transformation require higher energy input. Hydrogen as a high-energy material is commonly used for the large-scale catalytic transformation of CO_2 to value-added products [48-49]. These facts suggested an excellent heterogeneous catalyst with a lower activation barrier during the hydrogenation process along with the good ability in C–O bond scission and dissociation of hydrogen molecule (H_2) [50]. Enormous progress has been made in the synthesis of C1 molecules such as CH_3OH from CO_2 hydrogenation (under the "liquid sunshine" vision) [51] and has attracted massive interest in finding the optimal heterogeneous catalysts for CO_2 conversion [52-53]. CH_3OH has been industrially synthesized from syngas (CO/H_2) containing a small percentage of CO_2 using a $Cu/ZnO/Al_2O_3$ catalyst at harsh conditions (at 493−573 K and 5−10 MPa) [54]. Though the applicability of $Cu/ZnO/Al_2O_3$ catalyst at the industrial scale through the syngas route for converting CO_2 to CH_3OH directly is possible, it suffers from a series of technical problems such as low single-pass conversion, low methanol selectivity, requiring high pressure and fast deactivation by the reverse water gas shift (WGS) reaction [55].

Modifying the existing catalyst or developing new active catalysts for conditions with low the pressure and the temperature is an active field of research area [56]. Two main strategies are currently used to design new catalysts for CO_2 hydrogenation to CH_3OH and other products (1) conception of strong metal-support interaction (SMSI: metal/metal-oxide interfaces) to promote the formation of formate and thus increasing catalytic activity and selectivity and (2) engineering the coordination environment of active metal atoms by alloying [57-60] to control the reaction pathways that drive the chemical transformations. In agreement with the second tactic, bimetallic catalysts have shown enhanced activity and selectivity over single-component ones, as lattice engineering can be utilized to tailor the surface and electronic structure of bimetallic catalysts and thus to regulate their performance [61-63]. Various bimetallic materials

including Pd−Cu [64], Pd−Ga [65], Pd−In [66], Pd–Zn [67], Ni–Ga [68-69], In–Rh [70], In–Cu [71] In–Co [72], In–Ni [73] and Ni–Cu [74] have also been examined for methanol production from CO_2 hydrogenation. Among these materials, the Pd–Cu catalyst stands out as one of the most active bimetallic candidates for CH_3OH synthesis. Jiang et al. [75] proved that the Pd–Cu bimetallic catalysts possess a strong synergistic effect in the formation of CH_3OH as compared to that of pure Cu. Nørskov et al. [76] suggested the development of bimetallic Cu-based catalysts to break the scaling relationship and stabilize the reaction intermediate to lower the overpotential. Ma et al. [77] reported that the ordered Cu–Pd catalyst exhibits the highest selectivity for C1 products (> 80%). Meanwhile, catalysts based on noble metals such as Pd gain attention because of their good activity towards CH_3OH synthesis at lower temperatures in CO hydrogenation [78-79], where Cu-ZnO-based catalysts do not work well [79] in their aspects. The interactions and surface reactions on monometallic catalysts have been extensively studied, but little attention has been paid to Pd-Cu bimetallic catalysts. The rational design of highly efficient bimetallic catalysts demands a mechanistic insight into the catalytic CO_2 transformation processes on the active sites. At a certain level, the interplay between different metals and arrangement of respective metal atoms that alter catalyst properties is still a subject of great interest, including electronic structures, charge-transfer, and release of products, all of which influence catalytic performance [60]. The insightful investigations are further needed to identify the active sites and understand complete reaction networks for the selective catalytic conversion of CO_2 into hydrocarbons, such as HCOOH, CH_3OH, CH_4. The DFT calculations enable gas-phase studies of CO_2 reduction and hydrogenation to provide mechanistic insight into CO_2 functionalization at the molecular level [80-82]. Our work presented in chapter 3 highlights the combined effect of spin-polarization and inclusion of dispersion correction (D3) in examining the adsorbate-substrate relationship for CO oxidation [83]. As per our prior discussion in this chapter, Pd_5Cu_8 cluster stands out as an ideal model to

understand the hydrogenation process in terms of relative structural and energetic stability along with the optimum interaction with CO_2 in accordance with the Sabatier principle, as compared to mono or other bimetallic composition of Pd-Cu clusters [84]. In view of this, we pursue a systematic investigation of CO_2 hydrogenation reaction network to form HCOOH, CH_3OH, and CH_4 over Pd_5Cu_8 cluster using dispersion corrected spin-polarized density functional theory calculations. The kinetic energy barriers (E_a) and transition states for CO_2 hydrogenation were simulated by the climbing-image nudged elastic band (CI-NEB) method as implemented in Quantum Espresso [31,85-86]. Three images were used to mimic the reaction path. Similar convergence criteria and computational parameters (including the PBE+D3 approach) were adopted for the investigation of the reaction pathway as presented in section 4.2. The intermediate images were relaxed until the perpendicular force was less than 0.02 eV A^{-1}. The activation energy barrier (E_a) and reaction energy (ΔH) for each reaction step was obtained using the following formula,

$$E_a = E_{TS} - E_{IS} \tag{4.8}$$

$$\Delta H = E_{FS} - E_{IS} \tag{4.9}$$

where, E_{IS} , E_{TS} and E_{FS} respectively are energies of initial, transition states, and final states of the reaction. The reaction network presented in Figure 4.11 is considered to investigate the impact of Pd_5Cu_8 cluster on the activation and hydrogenation of CO_2 to HCOOH, CH_3OH, and CH_4. In Figure 4.11, the asterisk ($*$) indicates a species bound to the cluster, while the (g) represents a free molecule. The kinetic energy barriers of the corresponding elementary step are investigated by absorbing H* species adjacent to the intermediates. With reference to Figure 4.11, the activation of the CO_2 molecule from linear to bent configuration over the Pd_5Cu_8 cluster plus the dissociation of H_2 molecule are the critical steps for CO_2 hydrogenation. It was examined that the CO_2 molecule chemisorb over the Pd_5Cu_8 cluster in bent configuration with an adsorption energy -0.53 eV (see Table 4.3 and Figure 4.12). The adsorption energy corresponding to site preference, bond parameters of intermediate species are

presented in Table 4.3 and their pictorial representation is displayed in Figure 4.12. Löwdin charge analysis further reveals electrons transferred from cluster to the CO_2 molecule. The C–O bond is weakened and the CO_2 molecule is activated on Pd_5Cu_8 cluster. Next, the H_2 molecule chemisorbs over the Pd_5Cu_8 cluster in parallel configuration at the top site with -0.60 eV adsorption energy and dissociate into two H adatoms with an activation energy barrier of 0.43 eV (see Table 4.4 and Figure 4.13) which is an exothermic reaction with ΔH = -0.24 eV indicating a thermodynamically and kinetically favorable reaction. The values of activation energy barrier and reaction energy of elementary steps of CO_2 hydrogenation over Pd_5Cu_8 clusters are presented in Table 4.4. The pictorial representation of initial, transition, and final states of elementary steps of CO_2 hydrogenation over Pd_5Cu_8 cluster is depicted in Figure 4.13 and Figure 4.14. The adsorption energy of the H atom on the Pd_5Cu_8 cluster is -2.48 eV per H atom (relative to gaseous H_2). The weaker adsorption of H than CO_2 on the doped clusters would be beneficial for CO_2 fixation and hydrogenation.

The geometrical structure of Pd_5Cu_8 cluster is well maintained without notable deformation after CO_2 and H_2 chemisorption, manifesting the stability and robustness of this cluster. Therefore, the Pd_5Cu_8 cluster has superior chemical stability and high structural robustness under reaction conditions and is therefore eligible for CO_2 hydrogenation. The hydrogenation of CO_2* to form CO* and HCOOH* species can proceed through the carboxyl pathway (COOH*) and the formate pathway (HCOO*) via co-adsorption of CO_2* and H* over Pd_5Cu_8 cluster. The kinetic barrier for HCOO* (R3) formation (H* attacks the C atom of CO_2*) is 0.78 eV (with reaction energy -0.37 eV) which is higher than the value of COOH* formation (R2, H* attacks the O atom of CO_2*) i.e., 0.66 eV (Table 4.4), which corroborates that CO_2 reduction proceeds through the COOH* pathway is which more favorable to yield CH_3OH and CH_4. The hydrogenation of HCOOH* proceeds through the HCOO* pathway. This is expected due to the strong binding of the HCOO* as compared to COOH* over Pd_5Cu_8 cluster.

All the geometrical structures are well maintained with only little deformation during the reaction, indicating the robustness of Pd_5Cu_8 cluster (see Figure 4.12).

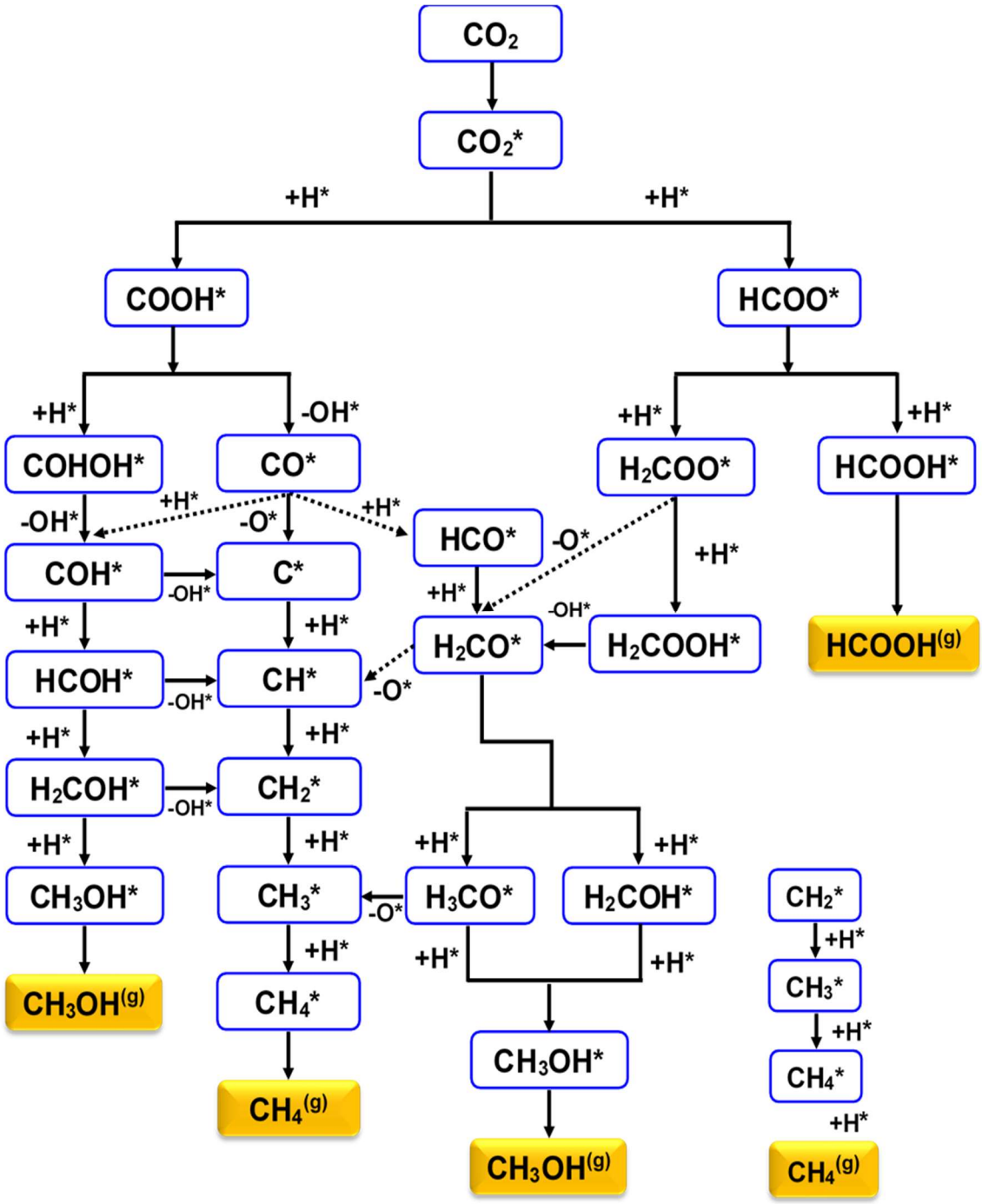

Figure 4.11: The possible reaction pathways of CO_2 hydrogenation to HCOOH, CH_3OH, and CH_4 on the Pd_5Cu_8 cluster. The symbol (*) and (g) indicates the adsorbed and gas phase species, respectively.

When the H* is combined with the O atom of HCOO* (R4), the HCOOH* is formed with an activation barrier of 0.78 eV with -0.37 eV reaction energy. The release

of HCOOH* (R5) from Pd_5Cu_8 cluster need 0.87 eV energy. As revealed in Figure 4.11, the COOH* can be decomposed into CO* and OH* (R6) or can also be hydrogenated to form COHOH* (R7). The COOH* decomposition is an exothermic reaction (-0.18 eV) with an activation barrier of 0.37 eV while the hydrogenation of COOH* to COHOH* exhibits a higher activation barrier of 1.28 eV, with a reaction energy of 0.71 eV. Thus, dissociation of COOH* is more likely to occur over the Pd_5Cu_8 cluster. However, CO is strongly chemisorbed over the Pd_5Cu_8 cluster with E_{ads} = -1.49 eV, hindering its desorption. Therefore, it is difficult to produce CO and the reversed water gas shift (RWGS) process is restricted, and the chemisorbed CO* can be further hydrogenated or dissociated to produce other C1 products. The hydrogenation product of CO* is HCO* or COH*, which depends on whether H* attacks the C or O atom of CO* (R8 or R9). From the kinetics point of view, HCO* formation is easy to occur over the Pd_5Cu_8 cluster due to the activation barrier of the R9 (2.55 eV) which is significantly higher than that of the R8 (1.18 eV). The direct dissociation of CO* (R10) is highly endothermic (ΔH = 2.85 eV) and has a higher activation barrier (3.19 eV). Then, HCO* is hydrogenated to form H_2CO* (R11) with a lower activation barrier (0.27 eV) and it is exothermic (ΔH = -0.33 eV). The hydrogenation of H_2CO* involves two competitive pathways: (1) the adsorbed H* attacks the C atom of H_2CO* to form H_3CO* (R13) and (2) the H* combines the O atom to form H_2COH* (R14). The formation of H_3CO* is more favorable attributed to the activation barrier of R13 which is 0.43 eV. This is 0.68 eV lower than that of R14. The activation barrier of 0.69 eV to dissociate H_3CO* into CH_3* + O* (R15) is almost equivalent to that of H_3CO* $\rightarrow$ CH_3OH* (R16, E_a = 0.68 eV). The hydrogenation of CH_3* to CH_4* has an activation barrier of 0.51 eV (R18). The produced H_2CO* is more likely to be further hydrogenated rather than to be decomposed (R12, E_a = 1.38 eV).

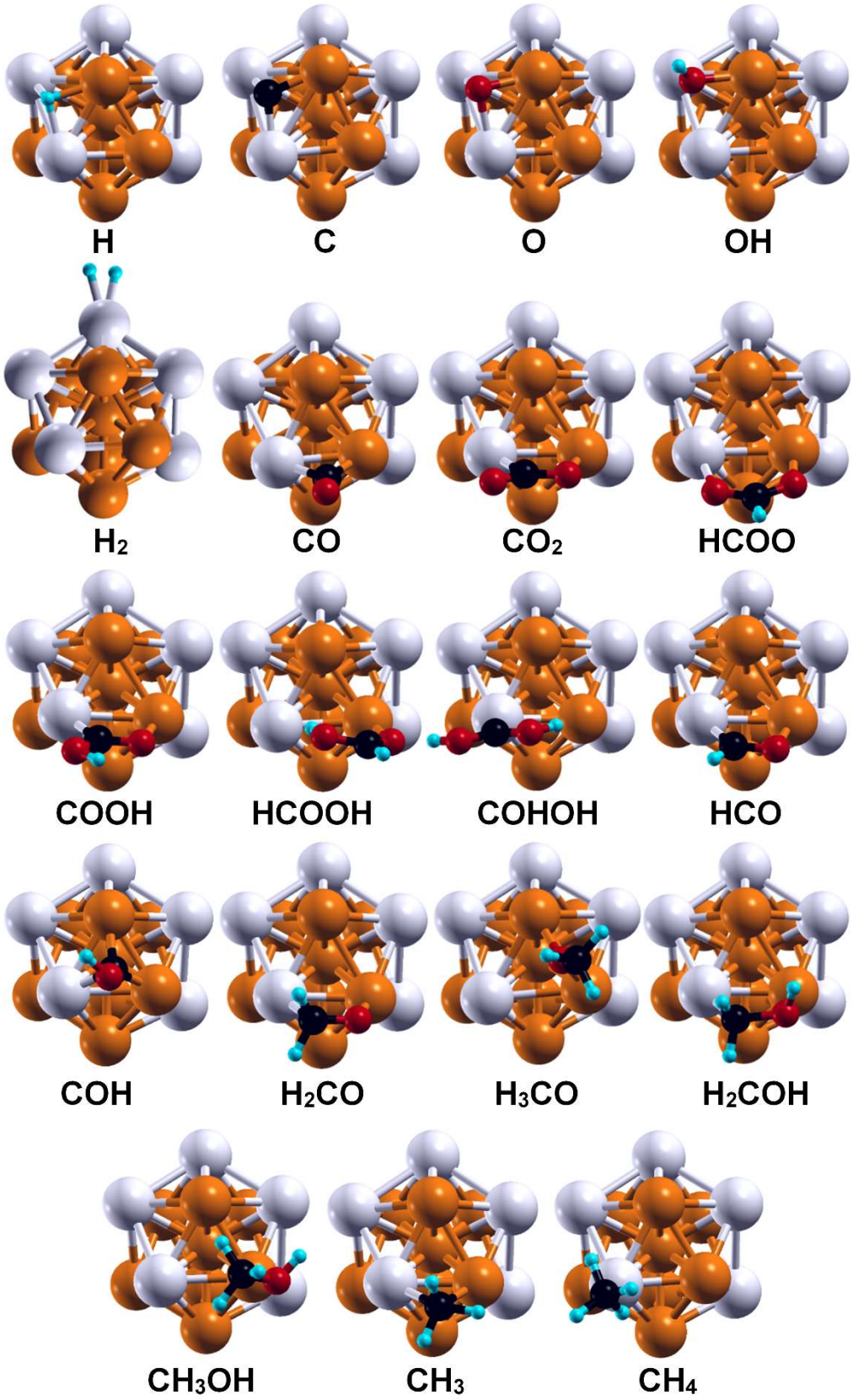

Figure 4.12: The low-lying adsorption configurations of intermediates in the hydrogenation of CO_2 on the Pd_5Cu_8 cluster. The white, orange, black, red, and cyan balls represent Pd, Cu, C, O, and H atoms, respectively.

Table 4.3: The most preferable adsorption site, bond parameters, and the adsorption energies (E_{ads}) of different species over the Pd_5Cu_8 cluster.

Species	Site	Bond-parameters (Å)	E_{ads} (eV)
H	H	$R_{H\text{-}Pd}$ = 1.80, 1.83 $R_{H\text{-}Cu}$ = 1.82	-2.48
C	H	$R_{C\text{-}Pd}$ = 1.89, 1.90 $R_{C\text{-}Cu}$ = 1.87	-5.87
O	H	$R_{O\text{-}Pd}$ = 2.04, 2.09 $R_{O\text{-}Cu}$ = 1.87	-4.52
OH	B	$R_{O\text{-}Pd}$ = 2.32 $R_{O\text{-}Cu}$ = 1.92	-2.97
H_2	T	$R_{H\text{-}Pd}$ = 1.75	-0.60
CO	B	$R_{C\text{-}Pd}$ = 2.00 $R_{C\text{-}Cu}$ = 1.95	-1.49
CO_2	B	$R_{C\text{-}Pd}$ = 2.02 $R_{O\text{-}Cu}$ = 2.01	-0.57
HCOO	B	$R_{O\text{-}Pd}$ = 2.12 $R_{O\text{-}Cu}$ = 1.94	-3.30
COOH	B	$R_{C\text{-}Pd}$ = 1.99 $R_{O\text{-}Cu}$ = 2.02	-2.53
HCOOH	T	$R_{O\text{-}Cu}$ = 2.00	-0.92
COHOH	T	$R_{C\text{-}Pd}$ = 1.98	-1.96
HCO	B	$R_{C\text{-}Pd}$ = 1.95, $R_{O\text{-}Cu}$ = 2.03	-2.28
COH	H	$R_{C\text{-}Pd}$ = 2.00, $R_{C\text{-}Cu}$ = 1.97, 1.92	-3.23
H_2CO	B	$R_{C\text{-}Pd}$ = 2.10 $R_{O\text{-}Cu}$ = 1.92	-1.10
H_3CO	B	$R_{O\text{-}Cu}$ = 1.97, 1.95	-2.51
H_2COH	B	$R_{C\text{-}Pd}$ = 2.05, $R_{C\text{-}Cu}$ = 2.08	-1.87
CH_3OH	T	$R_{O\text{-}Cu}$ = 2.10	-0.67
CH_3	B	$R_{C\text{-}Pd}$ = 2.16 $R_{C\text{-}Cu}$ = 2.15	-1.86
CH_4	T	$R_{C\text{-}Pd}$ = 2.74	-0.28

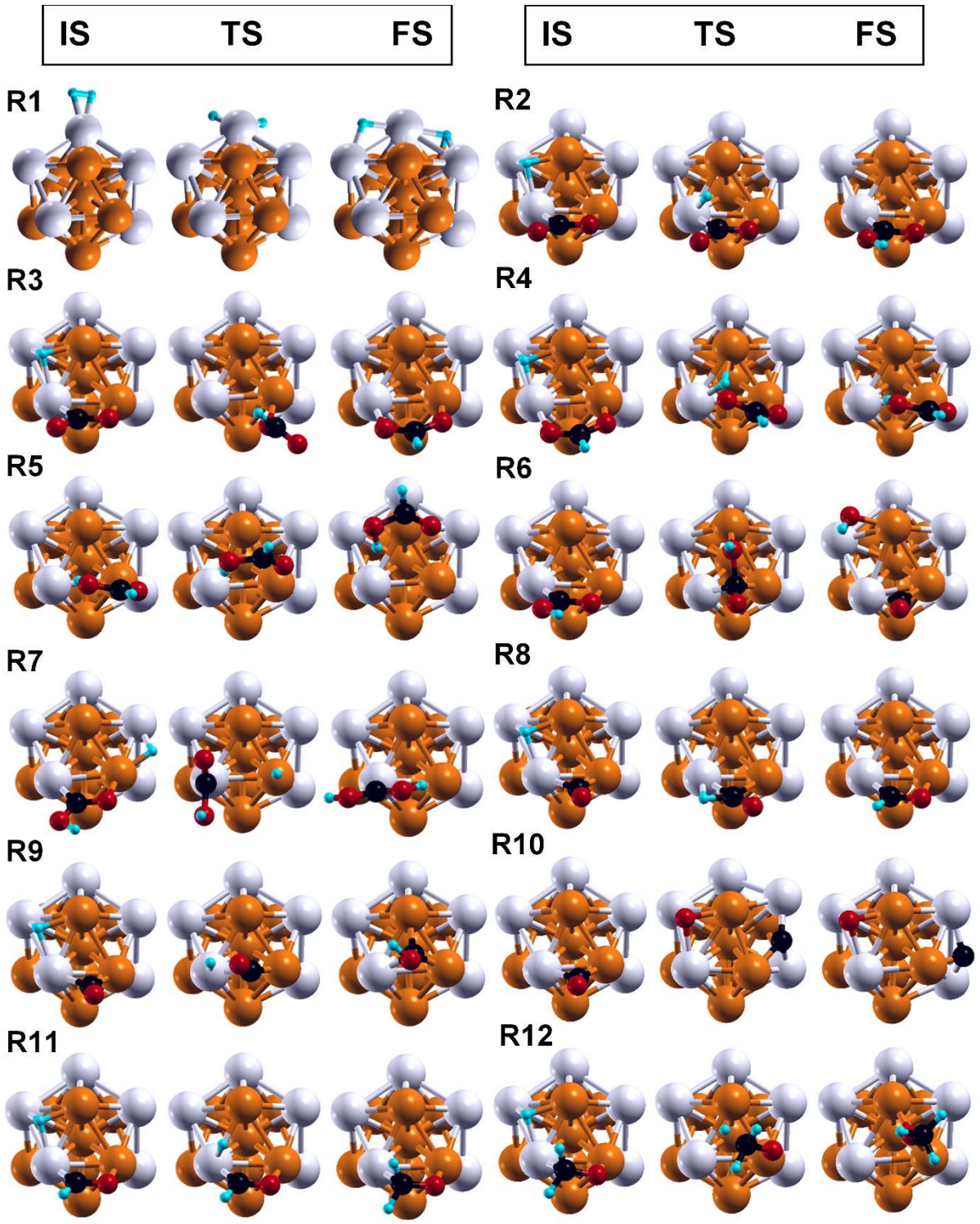

Figure 4.13: The initial state (IS), transition state (TS), and the final state (FS) of elementary step in CO_2 hydrogenation over the Pd_5Cu_8 cluster from R1 to R12.

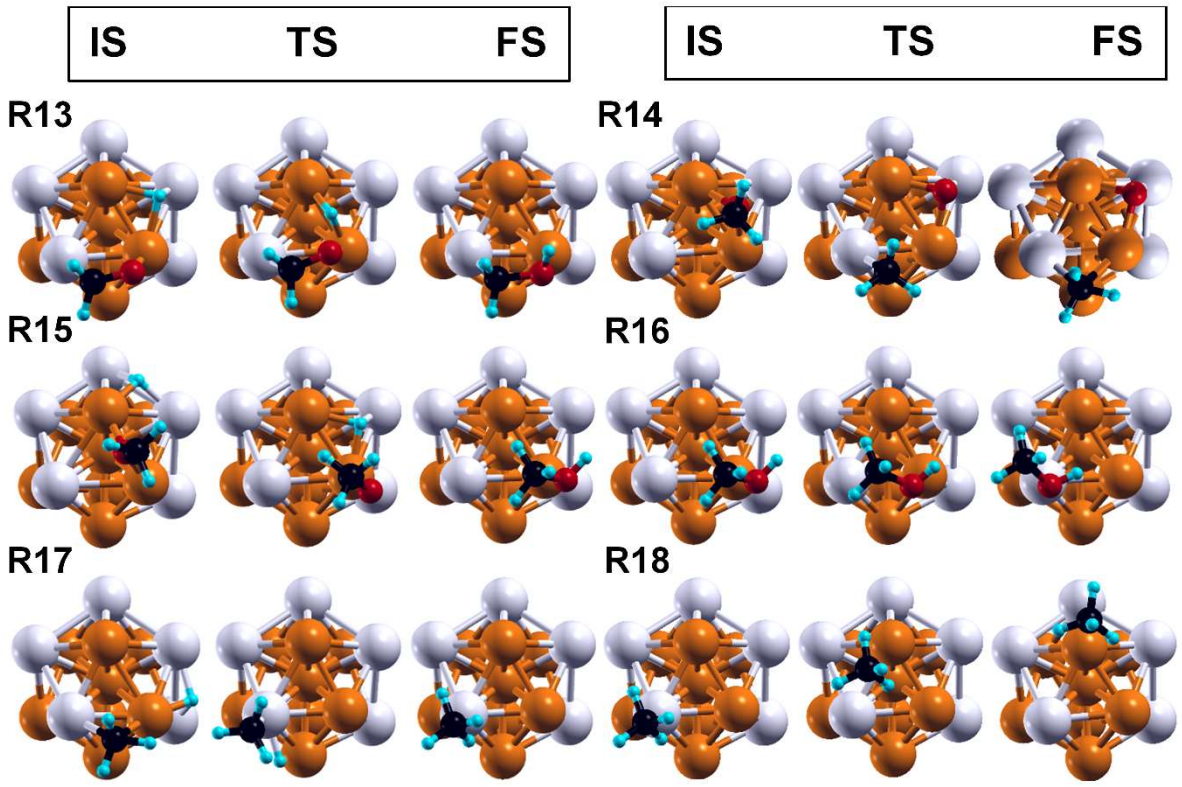

Figure 4.14: The initial state (IS), transition state (TS), and the final state (FS) of elementary step in CO_2 hydrogenation over the Pd_5Cu_8 cluster from R13 to R18

Finally, the ejection of CH_3OH^* (R17) and CH_4^* (R19) from the cluster requires an activation energy barrier of $E_a = 0.37$ eV and $E_a = 0.09$ eV, respectively. The optimized pathways for the production of HCOOH, CH_3OH, and CH_4 over the Pd_5Cu_8 cluster is presented in Figure 4.15. The rate-determining step for $HCOOH^{(g)}$ formation is HCOO* $\rightarrow$ HCOOH*. The rate-determining step for both $CH_3OH^{(g)}$ and $CH_4^{(g)}$ formation is CO* + H* $\rightarrow$ HCO* which involves a kinetic energy barrier of 1.18 eV. The Pd_5Cu_8 cluster exhibits the activity for all the C1 products with barriers of 0.27 eV – 1.18 eV. Based on the above analysis, Pd_5Cu_8 cluster possesses excellent activity and selectivity for CO_2 hydrogenation to various C1 products. The Pd_5Cu_8 cluster is more selective for CH_3OH, and also prefers to yield CH_4. The associated barriers for these major products are competitive to or even smaller than the previous theoretical values for Cu clusters and metal surfaces, e.g., 1.18 eV–1.69 eV for CH_3OH formation on the Cu_4 cluster supported on the Al_2O_3 substrate [87] and 1.41 eV on Cu [88-89] 1.17 eV for Au(111) to produce HCOOH [90] and 1.71 eV for Cu(111) to yield CH_4 [91].

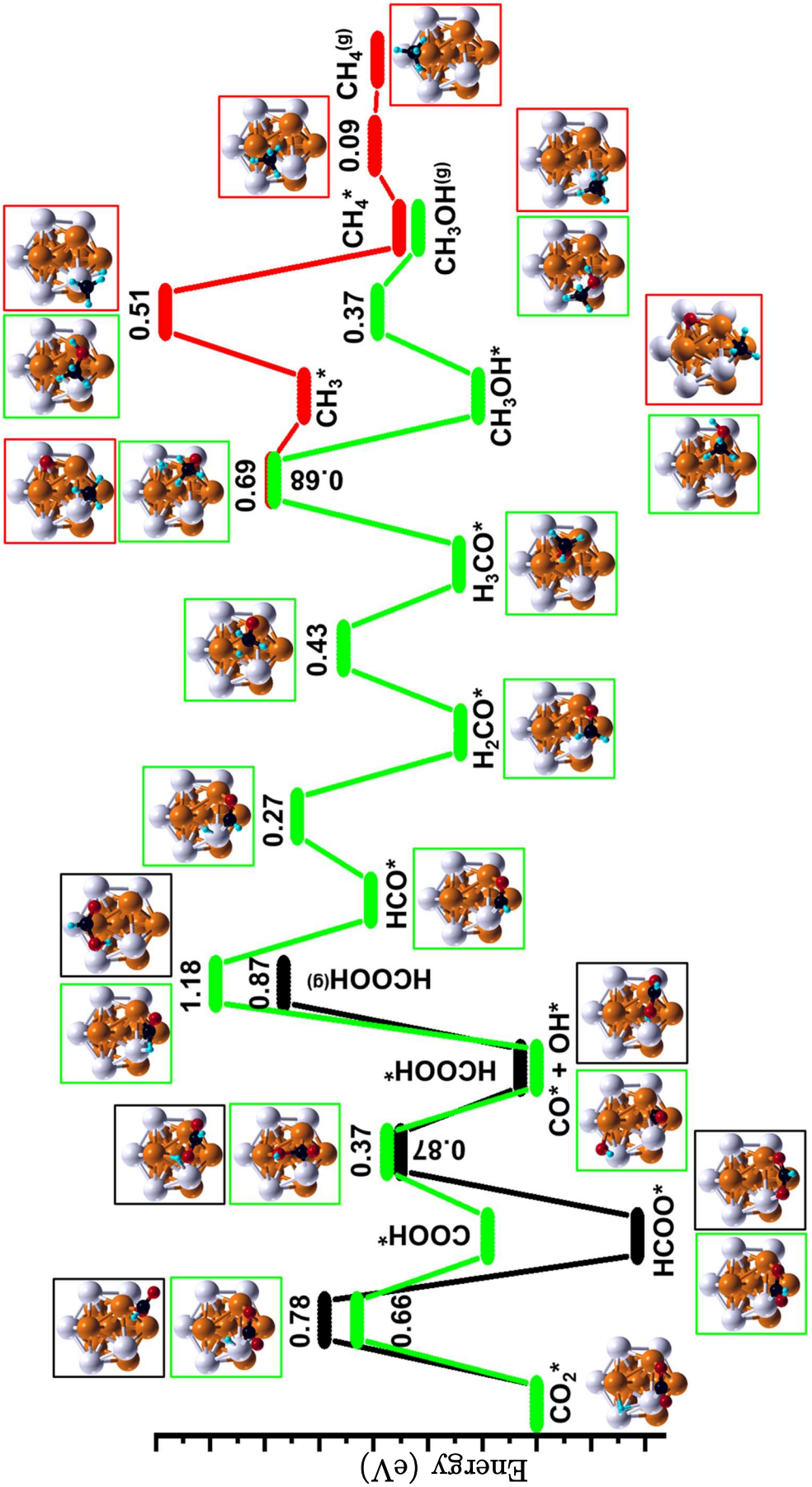

Figure 4.15: The optimized pathways for the production of HCOOH, CH_3OH, and CH_4 over the Pd_5Cu_8 cluster.

Table 4.4: Activation energy barriers (E_a, eV) and reaction energies (ΔH, eV) of elementary steps in CO_2 hydrogenation over the Pd_5Cu_8 cluster.

Reaction No.	Species	E_a	ΔH
R1	$H_2 + 2^* \rightarrow H^* + H^*$	0.43	-0.24
R2	$CO_2^* + H^* \rightarrow COOH^* + ^*$	0.66	0.18
R3	$CO_2^* + H^* \rightarrow HCOO^* + ^*$	0.78	-0.37
R4	$HCOO^* + H^* \rightarrow HCOOH^* + ^*$	0.87	0.43
R5	$HCOOH^* \rightarrow HCOOH$	-	0.87
R6	$COOH^* + ^* \rightarrow CO^* + OH^*$	0.37	-0.18
R7	$COOH^* + H^* \rightarrow COHOH^* + ^*$	1.28	0.71
R8	$CO^* + H^* \rightarrow HCO^* + ^*$	1.18	0.61
R9	$CO^* + H^* \rightarrow COH^* + ^*$	2.55	1.53
R10	$CO^* + ^* \rightarrow C^* + O^*$	3.19	2.85
R11	$HCO^* + H^* \rightarrow H_2CO^* + ^*$	0.27	-0.33
R12	$H_2CO^* + H^* \rightarrow H_3CO^* + ^*$	0.43	0.005
R13	$H_2CO^* + H^* \rightarrow H_2COH^* + ^*$	1.11	0.11
R14	$H_3CO^* + ^* \rightarrow CH_3^* + O^*$	0.69	0.57
R15	$H_3CO^* + H^* \rightarrow CH_3OH^* + ^*$	0.68	-0.07
R16	$CH_3OH^* \rightarrow CH_3OH$	0.37	0.22
R17	$CH_3^* + H^* \rightarrow CH_4^* + ^*$	0.51	-0.35
R18	$CH_4^* \rightarrow CH_4$	0.09	0.08

4.4 Conclusions

The conclusions drawn from the present theoretical study are underlined here. The structural stability (different composition of clusters) has been studied using the dispersion corrected DFT approach. Cu doped Pd clusters exhibit similar geometry to that of I_h Pd_{13} and Cu_{13} clusters. The presence of a Cu atom changes the stability of

the host cluster. Our results on average binding energy per atom (E_b), mixing energy (E_{mix}), second-order energy difference ($\Delta^2 E$) and average bond length ($\bar{R}$) confirm that the Cu-doped clusters are energetically more stable as compared to I_h Pd_{13} cluster. The negative values of mixing energy for all compositions of clusters are in favor of alloy formation for the whole range of compositions. The investigated stability factors imply that the I_h Pd_5Cu_8 cluster composition is highly stable (magic cluster) as compared to other cluster compositions.

To gain insights on the chemical enhancement of I_h Pd_mCu_n clusters, Raman spectra were obtained theoretically for individual I_h Pd_mCu_n clusters. The examined results of Raman spectra are in good agreement with the calculated results of structural stability and modulation in electronic structure. The maximum blue shift in the characteristic Raman peak is observed for I_h Cu_{13} cluster (at 486 cm^{-1}). Four different models of adsorption geometries are observed in the case of CO_2 molecule adsorption over I_h Pd_mCu_n clusters. The Löwdin charge calculation indicates that the electronic structure of Pd is altered due to the partial charge transfer from Cu to Pd. This modification in the electronic structure of Pd leads to the weak interaction between the I_h Pd_mCu_n clusters and CO_2 molecule and is meant to be accountable for the reduced CO_2 poisoning and enriched catalytic activity. In the charge density plots, enlargement of charge around O atom denotes that O atom plays the main role in the adsorption of CO_2 molecule as compared to carbon (C) owing to its higher electronegativity.

Our theoretical findings can be helpful to develop an understanding of the poisoning mechanism and chemisorption behavior of Pd and Cu-doped Pd alloy clusters with CO_2 gas molecule. For CO_2 hydrogenation over Pd_5Cu_8 cluster, the HCOOH is mainly produced by the reactions steps of $CO_2^* \rightarrow HCOO^* \rightarrow HCOOH^* \rightarrow HCOOH^{(g)}$. The rate-determining step is recognized as $HCOO^* \rightarrow HCOOH^*$, with an activation barrier of 0.78 eV. The CH_3OH and CH_4 is determined to be formed by the reactions of $CO_2^* \rightarrow COOH^* \rightarrow CO^* \rightarrow HCO^* \rightarrow H_2CO^* \rightarrow H_3CO^* \rightarrow CH_3OH^* \rightarrow CH_3OH^{(g)}$ and

CO_2* → COOH* → CO*→ HCO* → H_2CO* → H_3CO* → CH_3* + O* → CH_3 + H* → CH_4* → $CH_4^{(g)}$, respectively. These results offer an efficient strategy for precise tailoring of the catalytic behavior of the bimetallic Pd-Cu cluster and promote the development of a highly efficient catalyst for CO_2 hydrogenation.

References

1. Z. Luo, A. W. Castleman Jr., S. N. Khanna, *Chem. Rev.* **116**, 14456-14492, (2016).
2. K. Jalama, *Catal. Rev. Sci. Eng.* **59**, 95-164, (2017).
3. H. L. Kagdada, S. D. Dabhi, P. K. Jha, *Int. J. Hydrog. Energy* **43**, 21724-21731, (2018).
4. V. H. Mankad, S. K. Gupta, P. K. Jha, *AIP Conf. Proc.* **1731**, 090025-090027, (2016).
5. M. J. Piotrowski, P. Piquini, J. L. F. Da Silva, *Phys. Rev. B* **81**, 155446-155460, (2010).
6. C. J. Zhang, P. Hu, *J. Am. Chem. Soc.* **123**, 1166-1172, (2001).
7. S. Kunz, F. F. Schweinberger, V. Habibpour, M. Roettgen, C. Harding, M. Arenz, U. Heiz, J. *Phys. Chem. C* **114**, 1651-1654, (2010).
8. A. S. Worz, K. Judai, S. Abbet, U. Heiz, *J. Am. Chem. Soc.* **125**, 7964-7970, (2003).
9. S. Lee, B. Lee, F. Mehmood, S. Seifert, J. A. Libera, J. W. Elam, J. Greeley, P. Zapol, L. A. Curtiss, M. J. Pellin, et al., *J. Phys. Chem. C* **114**, 10342-10348, (2010).
10. S. Vajda, M. J. Pellin, J. P. Greeley, C. L. Marshall, L. A. Curtiss, G. A. Ballentine, J.W. Elam, S. Catillon-Mucherie, P. C. Redfern, F. Mehmood, et al., *Nature Mater.* **8**, 213-216, (2009).
11. X. Xing, A. Hermann, X. Kuang, M. Ju, C. Lu, Y. Jin, X. Xia, G. Maroulis, *Sci. Rep.* **6**, 19656-19667, (2016).
12. A. M. Köster, P. Calaminici, E. Orgaz, D. R. Roy, J. U. Reveles, S. N. Khanna, *J. Am. Chem. Soc.* **133**, 12192-12196, (2011).
13. C. Langhammer, I. Zoric, B. Kasemo, *Nano Lett.* **7**, 3122-3127, (2007).
14. P. Bera, K. C. Patil, V. Jayaram, G. N. Subbanna, M. S. Hegde, *J. Catal.* **196**, 293-301, (2007).
15. J. S. Filhol, M. Neurock, *Angew. Chem. Int. Ed.* **45**, 402-406, (2006).
16. J. N. Li, M. Pu, C. C. Ma, Y. Tian, J. He, D. G. Evans, *J. Mol. Catal. Chem.* **359**, 14-20, (2012).
17. I. V. Yudanov, R. Sahnoun, K. M. Neyman, N. Ro1sch, *J. Phys. Chem. B* **107**, 255-264, (2003).
18. Y. Gao, L. M. Zhang, C. C. Kong, Z. M. Yang, Y. M. Chen, *Chem. Phys. Lett.* **658**, 7-11, (2016).
19. X. Liu, D. Tian, C. Meng, *J. Mol. Struct.* **1080**, 105-110, (2015).

20. V. Bertani, C. Cavallotti, M. Masi, S. Carra, *J. Phys. Chem. A* **104**, 11390-11397, (2000).
21. C. Sousa, V. Bertin, F. Illas, *J. Phys. Chem. B* **105**, 1817-1822, (2001).
22. B. Fan, G. X. Ge, C. H. Jiang, G. H. Wang, J. G. Wan, *Sci. Rep.* **7**, 9539-9551, (2017).
23. M. Aslan, J. B. A. Davis, Roy L. Johnston, *Phys. Chem. Chem. Phys.* **18**, 6676-6682, (2016).
24. T. T. Li, C. He, W. X. Zhang, M. Cheng, *J. Alloys Compd.* **752**, 76-84, (2018).
25. D. Die, B. X. Zheng, L. Q. Zhao, Q. W. Zhu, Z. Q. Zhao, *Sci. Rep.* **6**, 31978-31991, (2016).
26. Y. Mu, Y. Han, J. Wang, J. G. Wan, G. Wang, *Phys. Rev. A* **84**, 053201-053208, (2011).
27. J. Wu, S. Shan, J. Luo, P. Joseph, V. Petkov, C. J. Zhong, *ACS Appl. Mater. Interfaces* **7**, 25906-25913, (2015).
28. M. J. Ren, Y. Zhou, F. F. Tao, Z. Q. Zou, D. L. Akins, H. Yang, *J. Phys. Chem. C* **118**, 12669-12675, (2014).
29. J. D. Cai, Y. Z. Zeng, Y. L. Guo, *J. Power Sources* **270**, 257-261, (2014).
30. A. G. Saputro, M. K. Agusta, T. D. K. Wungu, Suprijadi, F. Rusydi, H. K. Dipojono, *J. Phys. Conf.* **739**, 012083-012089, (2016).
31. P. Giannozzi, S. Baroni, N. Bonini, M. Calandra, R. Car, C. Cavazzoni, D. Ceresoli, G. L. Chiarotti, M. Cococcioni, I. Dabo, et al., *J. Phys.: Condens. Matter* **21**, 395502-395521, (2009).
32. G. Kresse, D. Joubert, Phys. Rev. B 59, 1758-1775, (1999).
33. J. P. Perdew, K. Burke, M. Ernzerhof, Phys. Rev. Lett. 77, 3865-3868, (1996).
34. N. Marzari, D. Vanderbilt, A. De Vita, M. C. Payne, *Phys. Rev. Lett.* **82**, 3296-3299, (1999).
35. J. D. Head, M. C. Zerner, *Chem. Phys. Lett.* **122,** 264-270, (1985).
36. A. Gross, Theoretical surface science: A microscopic perspective, Springer-Verlag, (2009).
37. S. Grimme, *J. Comput. Chem.* **27**, 1787-1799, (2006).
38. M. J. Frisch, G. W. Trucks, H. B. Schlegel, G. E. Scuseria, M. A. Robb, J. R. Cheeseman, G. Scalmani, V. Barone, B. Mennucci, G. A. Peterssonet, et al., Gaussian 09, Revision **D.01**, 1-20, (2013).
39. A. D. Becke, *Phys. Rev. A.* **33**, 2786-2788, (1986).
40. C. Lee, W. Yang, R.G. Parr, *Phys. Rev. B* **37**, 785-789, (1988).

41. B. Zhao, R. Zhang, Z. Huang, B. Wang, *Appl. Catal. A* **546**, 111-121, (2017).
42. M. Kabir, A. Mookerjee, A. K. Bhattacharya, *Eur. Phys. J. D.* **31**, 477-485, (2004).
43. R. Ferrando, J. Jellinek, R. L. Johnston, *Chem. Rev.* **108**, 845-910, (2008).
44. G. Rossi, A. Rapallo, C. Mottet, A. Fortunelli, F. Baletto, R. Ferrando, *Phys. Rev. Lett.* **93**, 105503-105507, (2004).
45. M. J. Piotrowski, P. Piquini, J. L. F. Da Silva, *J. Phys. Chem C* **116**, 18432-18439, (2012).
46. X. L. Lei, M. S. Wu, G. Liu, B. Xu, C. Y. Ouyang, *J. Phys. Chem. A* **117**, 8293-8297, (2013).
47. N. Austin, B. Butina, G. Mpourmpakis, *Pro. Nat. Sci. Mater.* **26**, 487-492, (2016).
48. Peng Gao, Lina Zhang, Shenggang Li, Zixuan Zhou, and Yuhan Sun, *ACS Cent. Sci.* **6**, 1657-1670, (2020).
49. W. Zhou, K. Cheng, J. C. Kang, C. Zhou, V. Subramanian, Q. H. Zhang, Y. Wang, *Chem. Soc. Rev.* **48**, 3193-3228, (2019).
50. Z. Ou, C. Qin J. Niu L. Zhang, J. Ran, *Int. J. Hydrog. Energy* **44**, 819, (2019).
51. C. F. Shih, T. Zhang, J. Li, C. Bai, *Joule* **2,** 1925-1949, (2018).
52. S. Dang, H. Yang, P. Gao, H. Wang, X. Li, W. Wei, Y. Sun, *Catal. Today* **330**, 61-75, (2019).
53. N. Podrojkova, V. Sans, A, Orinak, R. Orinakova, *Chem. Cat. Chem.* **12**, 1802-1825, (2020).
54. K. C. Waugh, *Catal. Today* **15**, 51-75 (1992).
55. U. J. Etim, Y. Song, Z. Zhong, *Front. Energy Res.* **8**, 545431-545457, (2020).
56. F. Brix, V. Desbuis, L. Piccolo, E. Gaudry, *J. Phys. Chem. Lett.* **11**, 7672-7678, (2020).
57. S. Kattel, P. Liu, J. G. Chen, *J. Am. Chem. Soc.* **139**, 9739-9754, (2017).
58. J. Graciani, K. Mudiyanselage, F. Xu, A. E. Baber, J. Evans, S. D. Senanayake, D. J. Stacchiola, P. Liu, J. Hrbek, J. Fernandez- Sanz, et al., *Science* **345**, 546-550, (2014).
59. S. Ma, M. Sadakiyo, M. Heima, R. Luo, R. T. Haasch, J. I. Gold, M. Yamauchi, P. J. A. Kenis, *J. Am. Chem. Soc.* **139**, 47-50, (2017).
60. G. Liu, P. Poths, X. Zhang, Z. Zhu, M. Marshall, M. Blankenhorn, A. N. Alexandrova, K. H. Bowen, *J. Am. Chem. Soc.* **142**, 7930-7936, (2020).
61. A. Vasileff, C. Xu, Y. Jiao, Y. Zheng, S.-Z. Qiao, *Chem.* **4**, 1809-1831, (2018).
62. K. D. Gilroy, A, Ruditskiy, H. C. Peng, D. Qin, Y. Xia. *Chem. Rev.* **116**, 10414-10472, (2016).

63. D. Kim, C. Xie, N. Becknell, Y. Yu, M. Karamad, K. Chan, E. J. Crumlin, J. K. Nørskov, P. J. Yang, *J. Am. Chem. Soc.* **139**, 8329-8336, (2017).
64. K. Mori, T. Sano, H. Kobayashi, H. Yamashita, *J. Am. Chem. Soc.* **140**, 8902-8909, (2018).
65. A. A. Garcia, E. Florez, A. Moreno, C. J Orozco, *Mol. Catal.* **484**, 110733-110742 (2020).
66. A. G. Trenco, E. R. White, A. Regoutz, D. J. Payne, M. S. P. Shaffer, C. K. Williams, *ACS Catal.* **7**, 1186-1196, (2017).
67. P. P. Wu, B. Yang, *Catal. Sci. Technol.* **9,** 6102-6113, (2019).
68. X. L. Li, G. L. Liu, D. Xu, X. L. Hong, S. C. E. Tsang, *J. Mater. Chem. A* **7**, 23878-23885, (2019).
69. F. Studt, I. Sharafutdinov, F. Abild-Pedersen, C. F. Elkjaer, J. S. Hummelshoj, S. Dahl, I. Chorkendorff, J. K. Nørskov, *Nat. Chem.* **6,** 320-324, (2014).
70. A, Gallo, J. L. Snider, D. Sokaras, D. Nordlund, T. Kroll, H. Ogasawara, L. Kovarik, M. S. Duyar, T. F. Jaramillo, *Appl. Catal., B* 267, 118369, (2020).
71. M. M. Li, H. Zou, J. Zheng, T. S. Wu, T. S. Chan, Y. L. Soo, X. P. Wu, X. Q. Gong, T. Chen, K. Roy, G. Held, S. C. E. Tsang, *Angew. Chem. Int. Ed.* **59**, 16039-16046, (2020).
72. Z. S. Shi, Q. Q. Tan, C. Tian, Y. Pan, X. W. Sun, J. X. Zhang, D. F. Wu, *J. Catal.* **379**, 78-89, (2019).
73. A. Pustovarenko, A. Dikhtiarenko, A. Bavykina, L. Gevers, A. Ramírez, A. Russkikh, S. Telalovic, A. Aguilar, J. L. Hazemann, S. Ould-Chikh, J. Gascon, *ACS Catal.* **10**, 5064-5076, (2020).
74. A. R. Richard, M. Fan, *Fuel* **222**, 513-522, (2018).
75. F. Z. Zhao, M. Gong, K. Cao, Y. H. Zhang, J. L. Li, R. Chen, *ChemCatChem,* **9**, 3772-3778, (2017).
76. X. Jiang, X. Nie, X. Wang, H. Wang, N. Koizumi, Y. Chen, X. Guo, C. Song, *J. Catal.* **369**, 21-32, (2019).
77. A. A. Peterson, J. K. Nørskov, *J. Phys. Chem. Lett.* **3**, 251-258, (2012).
78. A. Gotti, R. Prins, *J. Catal.* **175**, 302-311, (1998).
79. Y. Matsumura, W. J. Shen, Y. Ichihashi, M. Okumura, *J. Catal.* **197**, (2001) 267–272.
80. Q. J. Hong, Z. P. Liu, *Surf. Sci.* **604**, 1869-1876, (2010).
81. L. Grabow, M. Mavrikakis, *ACS Catal.* **1**, 365-384, (2011).

82. R. G. Zhang, B. J. Wang, H. Y. Liu, L. X. Ling, *J. Phys. Chem. C* 115, 19811-19818, (2011).
83. B. A. Baraiya, H. Tanna, V. Mankad, P. K. Jha, *J. Phys. Chem. A* **125**, 5256-5272, (2021).
84. B. A. Baraiya, V. Mankad, P. K. Jha, *Spectrochim. Acta A* **229**, 117912-117920, (2020).
85. G. Henkelman, H. Jónsson, *J. Chem. Phys.* **113**, 9978-9985, (2000).
86. G. Henkelman, B. P. Uberuaga, H. A. Jonsson, *J. Chem. Phys.* **113**, 9901-9904, (2000).
87. C. Liu, B. Yang, E. Tyo, S. Seifert, J. DeBartolo, B. von Issendorff, P. Zapol, S. Vajda, L. A. Curtiss, *J. Am. Chem. Soc.* **137**, 8676-8679, (2015).
88. Y. Yong, X. Su, Q. Zhou, Y. Kuang, X. Li, *Sci. Rep.* **7**, 17505-17517, (2017).
89. Y. Yang, J. Evans, J. A. Rodriguez, M. G. White, P. Liu, *Phys. Chem. Chem. Phys.* **12**, 9909-9917, (2010).
90. X. Lv, G. Lu, Z-Q. Wang, Z-N. Xu, G-C. Guo, *ACS Catal.* **7**, 4519-4526 (2017).
91. X. Nie, W. Luo, M. J. Janik, A. Asthagiri, *J. Catal.* **312**, 108-122 (2014).